Mechanical Systems and Signal Processing 211 (2024) 111199

Contents lists available at ScienceDirect

Mechanical Systems and Signal Processing

journal homepage: www.elsevier.com/locate/ymssp

Virtual model-aided reliability analysis considering material and geometrical uncertainties for elastic metamaterials

Minghui Zhang [a], Qihan Wang [a], Zhen Luo [b], Wei Gao [a,*]

[a] Centre for Infrastructure and Safety, School of Civil and Environmental Engineering, The University of New South Wales, Sydney, NSW 2052, Australia
[b] School of Mechanical and Mechatronic Engineering, The University of Technology Sydney, Sydney, NSW 2007, Australia

ARTICLE INFO

Keywords:
Elastic metamaterials
Bandgap analysis
Reliability analysis
Virtual modelling technique

ABSTRACT

Elastic metamaterials (EMMs) have enormous potential to be employed in real-world engineering, including transport, aerospace, civil engineering, due to their exceptional wave-manipulating capabilities. The system uncertainties raised by various factors in EMMs would lead to fluctuations in wave attenuation performance. Without thoroughly considering the system uncertainties, severe structural failure may occur. Thus, to provide possible access to quantifying the structural reliability involving material and geometrical uncertainties separately and simultaneously, a virtual model-aided framework is proposed. A recently developed virtual modelling technique, namely the Extended Support Vector Regression (X-SVR), has been adopted to generate virtual models, as alternatives to the original physical relationships between the system parameters and the concerned bandgap characteristics for EMMs. By implementing the sampling-based method on the established virtual models, sufficient statistical information and the structural reliability of concerned structural responses are estimated effectively and efficiently. In addition, the sensitivity analysis and information update can be easily executed on the established virtual models. Furthermore, the computational efficiency, accuracy, and robustness of the proposed virtual model-aided framework are demonstrated by numerical investigation. Convincingly, this advanced framework would significantly benefit the reliability-based analysis, design, and fabrication of EMMs in multi-disciplinary engineering applications.

1. Introduction

Elastic metamaterials (EMMs) with exotic properties [1], such as negative index of refraction [2], negative permeability [3], and negative permittivity [4], can be employed in a wide range of applications, including energy trapping, wave manipulation, acoustic clocking, wave guiding, which are attributed to their periodic structures with rationally designed unit cells [5–7]. One of the distinct attributes of EMMs is the capability to forbid the propagation of elastic waves due to the existence of bandgaps [8,9]. Bandgaps induced by the local resonance mechanism are capable of breaking the unit cell size limitation, offering significant merits over conventional materials in attenuating elastic waves at low frequencies [10]. Accordingly, locally resonant EMMs have been extensively investigated in recent years and are expected to possess great potential in various engineering disciplines, such as civil engineering, automotive, aerospace, biomechanics, etc. [11–13].

* Corresponding author.
E-mail address: w.gao@unsw.edu.au (W. Gao).

https://doi.org/10.1016/j.ymssp.2024.111199
Received 26 June 2023; Received in revised form 19 December 2023; Accepted 29 January 2024
Available online 10 February 2024

System uncertainty, as an inherent feature in real-world engineering, is underpinned within almost every component of the system, e.g., material property, structural geometry, and environment, attributed to heterogeneous sources, such as manufacturing, processing, measurements, and so on [14–17]. Convincingly, for EMMs, the bandgap characteristics are tightly related to the solid constituent and unit cell architecture; in other words, the system uncertainties can be reflected in the structural behavior. Without properly quantifying these effects on concerned structural responses, catastrophic structural failure may be caused. Hence, reliability analysis, concerning the probability of limit state violation, is an essential task for EMMs, in which the effects of the system uncertainties on the concerned structural response are thoroughly considered, and the structural reliability is estimated correspondingly [18–20].

With the consideration of randomness in the system parameters, solving the structural responses can be treated as a stochastic problem [21]. The structural reliability can be calculated from a multi-fold probability integral regarding the random structural response [22]. Nonetheless, analytically solving the random structural responses is infeasible for EMMs due to complex geometries, boundary conditions, and intractable access to all possible realizations of the random variables [23,24]. The stochastic finite element methods (SFEMs) provide alternative approaches to evaluate the random structural responses for EMMs [25,26]. As a straightforward technique with high robustness, the brute FEM-based Monte Carlo simulation (MCS) can be applied to execute reliability analysis for EMMs [27]. Besides, other popular SFEMs include the perturbation stochastic finite element method (PSFEM) and the spectral stochastic finite element method (SSFEM) [28]. By employing the PSFEM, the non-deterministic analysis of the concerned quantities (i.e., band structures, mode shapes, and frequency responses) for 2D acoustic metamaterials was carried out by He et al. [29]. Then, by adopting a spectral method based on generalized polynomial chaos (GPC), Henneberg et al. [30] investigated the statistical moments of the bandgap behaviors for a plate-type 2D EMM with the consideration of the geometrical uncertainties. Souf et al. [31] explored the effects of system uncertainties on the sound transmission loss for composite panels by adopting the GPC method. Later, Zakian et al. [32] proposed a stochastically enriched spectral FEM to investigate wave propagation in a 2D plate with structural randomness. Though great success has been achieved in stochastic analysis for different types of EMMs, to the best knowledge of the authors, most of the existing works are focused on the investigations for 1D and 2D structures. However, the implementation of 1D and 2D EMMs in real-life scenarios is very limited, attributed to the total failure to demonstrate the exotic properties in the perpendicular direction to the periodicity [33,34]. Since 3D EMMs have periodicity in three directions, they are capable of working more effectively and possessing significantly higher applicability in various engineering disciplines [92]. Nevertheless, the relevant studies on structural reliability for 3D EMMs are very limited.

Compared with 1D and 2D EMMs, tackling the structural reliability assessment for 3D EMMs is more challenging in both analytical and FEM-based approaches. The analytical method that can be employed to derive the deterministic dispersion relations for 1D and 2D EMMs fails on the 3D EMMs [35]. Such a dispirited conclusion is mainly induced by complex geometries, complicated boundary conditions, and sophisticated constitutive relationships [36]. When material and geometrical parameters are modelled as random variables in the system, the transformation of the deterministic problem into a non-deterministic problem further exaggerates the difficulty in analytically evaluating the structural responses. Rather than relying on an analytical approach, SFEMs provide alternatives to estimate random structural responses [37]. Even FEM-based MCS possesses high robustness and flexibility, the applicability of the brute MCS suffers severely, since accurate estimation of structural reliability generally requires large iterations [38,39]. It is especially challenging to be employed on 3D EMMs due to the large computational cost, since each deterministic bandgap analysis already requires sufficient computational resources [26,27]. Therefore, it is imperative to propose an alternative approach for evaluating the structural reliability of 3D EMMs in an efficient and effective manner.

Fortunately, with the blossoming of computer science, various virtual modelling techniques have been introduced to benefit the efficiency and effectiveness of stochastic structural analysis, structural reliability assessment, and structural health monitoring [40,41]. Typically, employing supervised virtual modelling techniques to reveal the implicit, underpinned, and sophisticated relationships between structural variables and dynamic responses for EMMs have gained tremendous popularity due to their highly efficient and accurate performance [42]. To benefit the applications of EMMs within various engineering disciplines, a virtual model-aided framework is proposed in this paper, aiming at systematically investigating the structural reliability of 3D EMMs in an efficient and effective manner.

Within the proposed framework, the core is adopting the virtual modelling technique to reveal the underpinned relationship between the system inputs and the concerned structural responses for 3D EMMs and establish effective virtual models correspondingly. To fulfil this task, a recently developed kernel-based virtual modelling technique, namely the extended support vector regression (X-SVR), is employed, which has been successfully implemented on reliability analyses for some engineering structures, including bar-type structures and building composites [23,42]. In addition, to improve the robustness of the X-SVR method, a new generalized kernel mapping function, namely the Automatic Relevance Determination - Generalized Eulerian kernel (ARD-GEK) is proposed, to serve as an additional option for the embedded X-SVR technique. By implementing the X-SVR virtual modelling technique, the implicit relationships between the system parameters and the structural responses are revealed based on a series of constrained optimization programming on the virtual models. Thus, instead of evaluating the sophisticated governing equations by FEM, the structural responses can be estimated based on explicit mathematical formulations. Thus, subsequent analysis based on the established virtual model can be implemented with extensively reduced computational costs. By integrating the MCS method with the established virtual models, a sufficient amount of statistical information, including means, standard deviations, probability density functions (PDFs), cumulative distribution functions (CDFs), and structural reliability can be estimated efficiently and effectively.

The remainder of the paper is organized as follows. The deterministic and reliability analyses of bandgap characteristics for 3D EMMs are illustrated in Sections 2.1 and 2.2, respectively. Section 3 introduces the detailed algorithms of the X-SVR method. The whole virtual model-aided framework is introduced in Section 4. Subsequently, to demonstrate the applicability, robustness, accuracy,

and efficiency of the proposed scheme, the structural reliability of a 3D lattice-based EMM is fully investigated in three numerical cases by considering material and geometrical uncertainties separately and simultaneously in Section 5. Finally, some conclusions are presented in Section 6.

2. Preliminaries

2.1. Deterministic analysis of bandgap characteristics for 3D EMMs

Bandgaps are endowed to EMMs and illustrations of 1D, 2D, and 3D EMMs are shown in Fig. 1.Compared with 1D and 2D EMMs, 3D EMMs exhibit periodicity in three directions and are capable of illustrating exceptional wave attenuation performance for waves from three directions. In EMMs, each unit cell interacts with adjacent cells [43,44]. Compared with 1D and 2D EMMs, each unit cell in 3D EMMs interacts with more neighboring cells. Since bandgap characteristics largely depend on interactions between unit cells [45,46], more interactions lead to more complex dispersion relations [43], which means that 3D EMMs generally have more complicated bandgap characteristics compared with 1D and 2D EMMs. To evaluate bandgap characteristics for 3D EMMs, a well-established theorem is employed, which is the Floquet-Bloch theorem [36,47–49]. Without loss of generality, the governing equation of elastic wave propagation in solids is given by [50]

$$\rho \frac{\partial^2 \mathbf{u}_i}{\partial^2 t^2} = \sum_{j=1}^{3} \frac{\partial}{\partial x_j} \left(\sum_{l=1}^{3} \sum_{k=1}^{3} c_{ijkl} \frac{\partial \mathbf{u}_\mathbf{k}}{\partial x_l} \right), (i = 1, 2, 3) \tag{1}$$

where ρ denotes the density of the material; $\mathbf{u}_i$ indicates the displacement vector; t denotes time; C_{ijkl} represents the elastic constant of the material; and x_j denotes the coordinate variables x, y, and z. To investigate the wave propagation behavior in an EMM with infinite unit cells, the Floquet-Bloch theorem is employed to solve Eq. (1). The solution can be written as:

$$\mathbf{u}(\mathbf{r}) = \mathbf{u}_\mathbf{k}(\mathbf{r}) e^{i(\mathbf{k}\cdot\mathbf{r})} \tag{2}$$

where $\mathbf{r}(x, y, z)$ denotes the position vector and $\mathbf{k}(k_x, k_y, k_z)$ represents the Bloch wave vector. With the Floquet-Bloch periodicity condition applied in the x, y, and z directions, the components of displacement $\mathbf{u}(\mathbf{r})$ can be written as [49]:

$$u(x + a, y, z) = u(x, y, z) e^{i(k_x \cdot a)} \tag{3}$$

$$u(x, y + a, z) = u(x, y, z) e^{i(k_y \cdot a)} \tag{4}$$

$$u(x, y, z + a) = u(x, y, z) e^{i(k_z \cdot a)} \tag{5}$$

where a is the lattice constant of the EMM. The passband and bandgap can be identified by solving the dispersion relation which is an implicit function between the wavevector and the eigenfrequency. By substituting the Eqs. (3)–(5) into Eq. (1), the dispersion relations of infinite 3D EMMs can be obtained by solving the eigenvalue problem:

$$\left(\mathbf{\Gamma} - \boldsymbol{\omega}^2(\mathbf{k})\mathbf{M}\right)\mathbf{u} = 0 \tag{6}$$

where $\mathbf{\Gamma}$ denotes the stiffness matrix, and $\mathbf{M}$ represents the mass matrix. By substituting the periodic boundary conditions of Eqs. (3)–(5) into Eq. (6), the solution set $\boldsymbol{\omega}(\mathbf{k})^*$ can be written as:

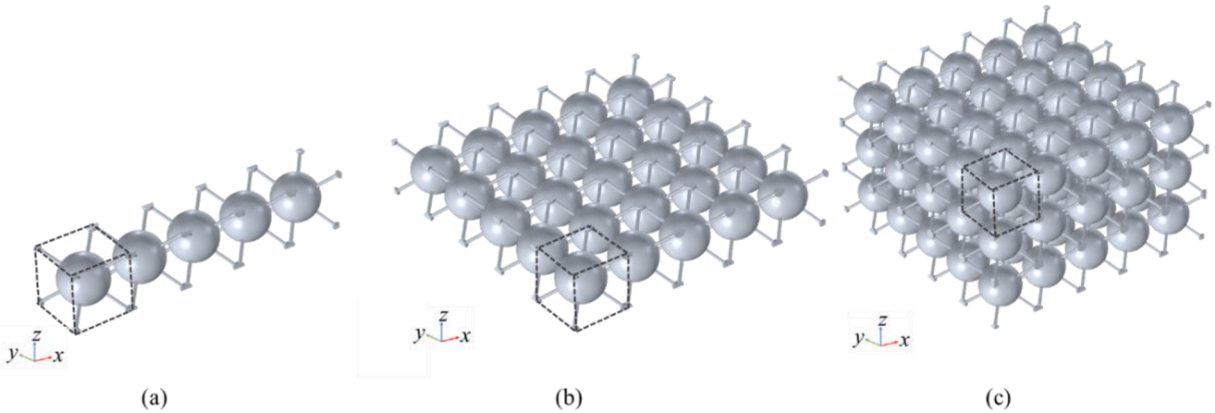

Fig. 1. (a) 1D EMM, (b) 2D EMM, and (c) 3D EMM.

$$\boldsymbol{\omega}(\mathbf{k})^{*} = \left\{\boldsymbol{\omega}_1(\mathbf{k}), \boldsymbol{\omega}_2(\mathbf{k}), ..., \boldsymbol{\omega}_p(\mathbf{k}), ..., \boldsymbol{\omega}_d(\mathbf{k})\right\} \tag{7}$$

in which d denotes the degrees of freedom (DoF) of the models in FEM. Subsequently, the bandgap properties of the EMM can then be obtained by sweeping the wavevector $\mathbf{k}$ along the first Brillouin path [51]. The complete bandgap is identified, which has no eigenfrequency falling into the frequency range along the whole $\mathbf{k}$-path. Since the first bandgap is mostly concerned and the investigation about it can be easily extended to subsequent bandgaps over higher frequencies. Thus, in this research, the reliability analysis focuses on the investigation of the 1st bandgap, which is characterized by two quantities, i.e., the starting frequency (f_s) and the cut-off frequency (f_c). The 1st bandgap is identified by finding the lowest p denoted as $p_{\min}$, satisfying $\min\left(\boldsymbol{\omega}_{p_{\min}+1}(\mathbf{k})\right) - \max\left(\boldsymbol{\omega}_{p_{\min}}(\mathbf{k})\right) > 0$. Then, the concerned f_s and f_c can be calculated as:

$$f_s = \frac{\max\left(\boldsymbol{\omega}_{p_{\min}}(\mathbf{k})\right)}{2\pi} \tag{8}$$

$$f_c = \frac{\min\left(\boldsymbol{\omega}_{p_{\min}+1}(\mathbf{k})\right)}{2\pi} \tag{9}$$

2.2. Reliability analysis of bandgap characteristics for 3D EMMs

In real-life engineering, system uncertainty is inherently existing within material properties, structural geometries, load conditions, and environments [52,53]. These system uncertainties would significantly affect the structural performance and numerous engineering accidents have repeatedly raised the warning on structural safety [54]. Thus, appropriate access to structural reliability is always an essential task in engineering applications [55]. Especially for EMMs, such an advanced material developed in recent years, sufficient exploratory research on its various physical performance is vital. Therefore, the reliability analysis for 3D EMMs by considering both material and geometrical uncertainties has been thoroughly investigated in this research.

Without loss of generality, let $\boldsymbol{\xi}^{\mathrm{R}}$ denotes the random vector, which collects all uncertain systematic input parameters ξ_{ℓ}^{R}, for $\ell = 1, 2, ..., n$ in a probability space $(\boldsymbol{\Omega}, \boldsymbol{\Lambda}, \mathbf{P})$. The governing equation of the random dispersion relation for 3D EMMs is formulated as:

$$\begin{cases} \left(\boldsymbol{\Gamma}\left(\boldsymbol{\xi}^{\mathrm{R}}\right) - \left(\boldsymbol{\omega}^{\mathrm{R}}(\mathbf{k})\right)^{2}\mathbf{M}\left(\boldsymbol{\xi}^{\mathrm{R}}\right)\right)\mathbf{u}^{\mathrm{R}} = 0 \\ \boldsymbol{\xi}^{\mathrm{R}} \in \boldsymbol{\Omega} := \left\{\boldsymbol{\xi}^{\mathrm{R}} \in \Re^{n} \middle| \xi_{\ell}^{\mathrm{R}} \sim f^{\mathrm{D}}_{\xi_{\ell}^{\mathrm{R}}}(x), \text{for } \ell = 1, 2, ..., n\right\} \end{cases} \tag{10}$$

where $\boldsymbol{\Gamma}\left(\boldsymbol{\xi}^{\mathrm{R}}\right) \in \Re^{d\times d}$ and $\mathbf{M}\left(\boldsymbol{\xi}^{\mathrm{R}}\right) \in \Re^{d\times d}$ indicate the random stiffness matrix and mass matrix, respectively, which are functions of the random vector $\boldsymbol{\xi}^{\mathrm{R}}$; $\Re$ indicates a real number; $\mathbf{u}^{\mathrm{R}}$ and $\boldsymbol{\omega}^{\mathrm{R}}(\cdot) \in \Re^{d}$ denote the random displacement vector and solution of the dispersion relation, respectively; $\boldsymbol{\xi}^{\mathrm{R}} \in \Re^{n}$ is an n-dimensional vector consisting of all system parameters modelled as random variables. The corresponding probability density function (PDF) for the ℓth random variable ξ_{ℓ}^{R} is $f^{\mathrm{D}}_{\xi_{\ell}^{\mathrm{R}}}(x)$. By considering system properties as random variables, concerned bandgap characteristics i.e., f_s and f_c possess the features of randomness, which can be functionally respectively expressed as,

$$f_s^{\mathrm{R}} = F_s\left(\boldsymbol{\omega}^{\mathrm{R}}(\mathbf{k})\right) = \widehat{F}_s\left(\boldsymbol{\xi}^{\mathrm{R}}\right) \tag{11}$$

$$f_c^{\mathrm{R}} = F_c\left(\boldsymbol{\omega}^{\mathrm{R}}(\mathbf{k})\right) = \widehat{F}_c\left(\boldsymbol{\xi}^{\mathrm{R}}\right) \tag{12}$$

where f_s^{R} and f_c^{R} represent random starting and cut-off frequencies, respectively; $F_s(\bullet)$ and $\widehat{F}_s(\bullet)$ denote the functional expressions from $\boldsymbol{\omega}^{\mathrm{R}}(\mathbf{k})$ and $\boldsymbol{\xi}^{\mathrm{R}}$ to f_s^{R}, respectively; $F_c(\bullet)$ and $\widehat{F}_c(\bullet)$ represent the functional expressions from $\boldsymbol{\omega}^{\mathrm{R}}(\mathbf{k})$ and $\boldsymbol{\xi}^{\mathrm{R}}$ to f_c^{R}, respectively. To avoid the repetition in the manuscript, only the limit-state function (LSF) for the concerned bandgap characteristics f_s^{R} is presented, which is similar to f_c^{R} in expression. Specifically, the LSF for f_s^{R} is represented as $G\left(f_s^{\mathrm{R}}\right)$ defined as $G\left(f_s^{\mathrm{R}}\right) = f_s^{*} - f_s^{\mathrm{R}}$, where f_s^{*} indicates the capacity of the system and is generally referred to as a deterministic parameter. Based on that, the safe region and the failure region are defined as $\Theta_s := \left\{f_s^{\mathrm{R}} \in \Re | G\left(f_s^{\mathrm{R}}\right) > 0\right\}$ and $\Theta_f := \left\{f_s^{\mathrm{R}} \in \Re | G\left(f_s^{\mathrm{R}}\right) < 0\right\}$, respectively. Therefore, the structural reliability is defined as a multi-fold probability integral function:

$$P_r = Pr\left(G\left(f_s^{\mathrm{R}}\right) \geqslant 0\right) = Pr\left(f_s^{\mathrm{R}} \leqslant f_s^{*}\right) = \int\int \cdots \int_{f_s^{\mathrm{R}} \leqslant f_s^{*}} f^{\mathrm{D}}_{f_s^{\mathrm{R}}}(x)dx \tag{13}$$

where $Pr(\bullet)$ and $f^{\mathrm{D}}_{(\bullet)}(x)$ denote the probability and the PDF of $(\bullet)$, respectively. To the best knowledge of the authors, analytically investigating structural reliability for 3D EMMs is theoretically infeasible, which is attributed to three main reasons. First, higher-order eigenmodes for 3D EMMs cannot be analytically solved, especially for unit cells with complex geometries [36]. With the introduction of system uncertainties, the deterministic eigenvalue problem transforms into a stochastic eigenvalue problem, and thus the difficulty surges significantly in analytical approaches. Secondly, due to the high dimensionality and nonlinearity, the multi-fold probability integral function is infeasible to be analytically solved directly [23,56]. The third reason is that it is computationally inaccessible to

solve all possible solutions for dispersion relations $\boldsymbol{\omega}^{\mathrm{R}}(\mathbf{k})$, since there are infinite realizations and assemblies for random inputs [57,58].

Instead of relying on analytical approaches, brute MCS, i.e., FEM coupled with MCS, is a brute-force strategy with high robustness to estimate random structural responses for engineering structures [59]. However, large iterations of MCS are generally required to accurately estimate random structural responses [60]. It is especially challenging when the method is implemented on 3D EMMs, since solving a deterministic bandgap analysis has already been computationally expensive [38,61]. By considering the geometrical uncertainty, this dilemma would be further aggravated. In each realization, remeshing and reassembling the stiffness and mass matrixes would become inevitable, which further increases the computational burden. Another commonly adopted intrusive method to tackle stochastic analysis is the PSFEM [25]. In the implementation of PSFEM, the estimation of a random solution requires to access the system stiffness matrix, which is computationally ineffective when the structural discretization is altered [62,63]. In addition, since this method relies on a low-degree polynomial approximation of the structural response, the accuracy of the result suffers significantly when the uncertainties are in high variability levels to the nominal values [64]. Another popular SFEM is SSFEM [65]. Nonetheless, due to its inherent characteristics, the stiffness system matrix needs to be expanded along each of the random input dimensions [66]. Hence, the stiffness matrix size is increased in order compared with the one in the deterministic analysis, implying a tremendous computational cost, especially for the complicated 3D EMMs with large numbers of DoF [28].

Therefore, to provide possible accesses to tackle these challenges in structural reliability assessment for 3D EMMs, a virtual modal-aided framework, i.e., a metamodeling-based MCS with high robustness is developed. Before introducing the whole analysis framework, a recently developed supervised regression technique is introduced in Section 3, to bridge the implicit relationships between system parameters and the concerned structural responses.

3. Virtual model construction

3.1. Extended support vector regression (X-SVR)

To significantly reduce the computational cost in estimating the structural responses, the underpinned constitutive relationships are substituted by explicit formulations, through a virtual modelling technique, namely the extended support vector regression (X-SVR). Hence, by implementing the MCS on the established virtual model instead of the FEM model, the required computational resources are sharply reduced. In the embedded X-SVR technique, a quadratic ε-insensitive loss function $l_2^{\varepsilon}(\bullet)$ introduced in Eq. (14) replaces the linear ε-insensitive function in the conventional SVR to improve the numerical stability.

$$l_2^{\varepsilon}(Y_i - \widehat{f}(\mathbf{X}_i)) = |Y_i - \widehat{f}(\mathbf{X}_i)|^2, \text{ for } i = 1, 2, \ldots, m \tag{14}$$

where $\mathbf{X}_{\text{train}} = [\mathbf{X}_1, \mathbf{X}_2, \ldots, \mathbf{X}_i]^{\mathrm{T}} \in \Re^{m\times n}$ and $\mathbf{Y}_{\text{train}} = [Y_1, Y_2, \ldots, Y_i]^{\mathrm{T}} \in \Re^{m}$ are inputs and corresponding outputs in the training datasets, respectively; $\widehat{f}(\mathbf{X}_i)$ denotes the established virtual models; m denotes the number of realizations for the random inputs. Accordingly, the governing formulation for the linear X-SVR technique can be expressed as:

$$\min_{\mathbf{p},\mathbf{q},\delta,\boldsymbol{\xi},\boldsymbol{\xi}^*} : \left(\|\mathbf{p}\|_2^2 + \|\mathbf{q}\|_2^2\right) + \lambda \mathbf{e}_n^{\mathrm{T}}(\mathbf{p}+\mathbf{q}) + \frac{C}{2}\left(\boldsymbol{\xi}^{\mathrm{T}}\boldsymbol{\xi} + \boldsymbol{\xi}^{*\mathrm{T}}\boldsymbol{\xi}^*\right) \tag{15}$$

$$s.t. \begin{cases} \mathbf{X}_{\text{train}}(\mathbf{p}-\mathbf{q}) + \delta\mathbf{e}_m - \mathbf{Y}_{\text{train}} \leqslant \varepsilon\mathbf{e}_m + \boldsymbol{\xi} \\ \mathbf{Y}_{\text{train}} - \mathbf{X}_{\text{train}}(\mathbf{p}-\mathbf{q}) - \delta\mathbf{e}_m \leqslant \varepsilon\mathbf{e}_m + \boldsymbol{\xi}^* \\ \mathbf{p}, \mathbf{q} \geqslant \mathbf{0}_n; \boldsymbol{\xi}, \boldsymbol{\xi}^* \geqslant \mathbf{0}_m \end{cases} \tag{16}$$

where $\lambda \in \Re^+$ indicate a tuning parameter for balancing the performance of regression and feature selection; $\boldsymbol{\xi}, \boldsymbol{\xi}^* \in \Re^m$ denote two non-negative vectors; $\mathbf{e}_n = [1, 1, \ldots, 1]^{\mathrm{T}} \in \Re^n$ and $\mathbf{0}_n = [0, 0, \ldots, 0]^{\mathrm{T}} \in \Re^n$ represent the ones vector and the zeros vector, respectively; $\mathbf{p}, \mathbf{q} \in \Re^n$ are two negative variables [67]; C denotes a penalty constant.

The physical relationships between system parameters, i.e., material properties and geometrical parameters, and dispersion relations are sophisticated, especially for higher-order eigenfrequencies in 3D EMMs. Therefore, directly developing effective virtual models via a linear X-SVR technique on the input features is infeasible. To accurately estimate the structural responses, a nonlinear regression is requisite to be established [23]. This is achieved by mapping the raw input data from the low-dimensional space $\Re^n$ into a higher-dimensional Euclidian space or even infinite dimensional Hilbert feature space by an empirical mapping function $\boldsymbol{\Phi}(\mathbf{X}_i)$. The implementation of the empirical mapping on $\mathbf{X}_i$ is written as:

$$\mathbf{X}_i = \left[X_{i,1}, X_{i,2}, \ldots, X_{i,n}\right]^{\mathrm{T}} \rightarrow \widehat{\kappa}(\mathbf{X}_i) = \begin{bmatrix} \boldsymbol{\Phi}(\mathbf{X}_1)^{\mathrm{T}}\boldsymbol{\Phi}(\mathbf{X}_i) \\ \boldsymbol{\Phi}(\mathbf{X}_2)^{\mathrm{T}}\boldsymbol{\Phi}(\mathbf{X}_i) \\ \vdots \\ \boldsymbol{\Phi}(\mathbf{X}_m)^{\mathrm{T}}\boldsymbol{\Phi}(\mathbf{X}_i) \end{bmatrix} = \begin{bmatrix} \kappa(\mathbf{X}_1, \mathbf{X}_i) \\ \kappa(\mathbf{X}_2, \mathbf{X}_i) \\ \vdots \\ \kappa(\mathbf{X}_m, \mathbf{X}_i) \end{bmatrix}, \text{ for } i = 1, 2, \cdots m \tag{17}$$

where the empirical feature vector $\widehat{\kappa}(\mathbf{X}_i)$ is the ith empirical feature vector with the empirical degree of m, which is a m-dimensional vector space that is referred as the empirical feature space. In addition, $\widehat{\kappa}(\mathbf{X}_i)$ is the ith training input for developing the nonlinear virtual model. By virtue of a kernel function $\kappa(\bullet, \bullet)$, the original training input datasets $\mathbf{X}_{\text{train}}$ can be converted into a kernel matrix that can be written as:

$$\boldsymbol{\kappa}_{\text{train}} = \begin{bmatrix} \kappa(\mathbf{X}_1, \mathbf{X}_1) & \kappa(\mathbf{X}_1, \mathbf{X}_2) & \cdots & \kappa(\mathbf{X}_1, \mathbf{X}_m) \\ \kappa(\mathbf{X}_2, \mathbf{X}_1) & \kappa(\mathbf{X}_2, \mathbf{X}_2) & \cdots & \kappa(\mathbf{X}_2, \mathbf{X}_m) \\ \vdots & \vdots & \ddots & \vdots \\ \kappa(\mathbf{X}_m, \mathbf{X}_1) & \kappa(\mathbf{X}_m, \mathbf{X}_2) & \cdots & \kappa(\mathbf{X}_m, \mathbf{X}_m) \end{bmatrix} \in \Re^{m \times m} \tag{18}$$

By using $\boldsymbol{\kappa}_{\text{train}}$ as the training input dataset, the nonlinear X-SVR optimization problem can be expressed as:

$$\min_{\mathbf{p},\mathbf{q},\delta,\boldsymbol{\xi},\boldsymbol{\xi}^*} : \left(\|\mathbf{p}\|_2^2 + \|\mathbf{q}\|_2^2\right) + \lambda \mathbf{e}_n^{\mathrm{T}}(\mathbf{p}+\mathbf{q}) + \frac{C}{2}\left(\boldsymbol{\xi}^{\mathrm{T}}\boldsymbol{\xi} + \boldsymbol{\xi}^{*\mathrm{T}}\boldsymbol{\xi}^*\right) \tag{19}$$

$$s.t. \begin{cases} \boldsymbol{\kappa}_{\text{train}}(\mathbf{p}-\mathbf{q}) + \delta\mathbf{e}_m - \mathbf{Y}_{\text{train}} \leqslant \varepsilon\mathbf{e}_m + \boldsymbol{\xi} \\ \mathbf{Y}_{\text{train}} - \boldsymbol{\kappa}_{\text{train}}(\mathbf{p}-\mathbf{q}) - \delta\mathbf{e}_m \leqslant \varepsilon\mathbf{e}_m + \boldsymbol{\xi}^* \\ \mathbf{p}, \mathbf{q} \geqslant \mathbf{0}_n, \boldsymbol{\xi}, \boldsymbol{\xi}^* \geqslant \mathbf{0}_m \end{cases} \tag{20}$$

Subsequently, the optimization problem in Eqs. (15) and (16) can be simplified as:

$$\min_{\widehat{\mathbf{z}},\delta} : \frac{1}{2}\left(\widehat{\mathbf{z}}^{\mathrm{T}}\widehat{\mathbf{C}}\widehat{\mathbf{z}} + \delta^2\right) + \lambda\widehat{\mathbf{a}}^{\mathrm{T}}\widehat{\mathbf{z}} \tag{21}$$

$$s.t. (\widehat{\mathbf{A}} + \mathbf{I}_{4m})\widehat{\mathbf{z}} + (\varepsilon\mathbf{I}_{4m} + \delta\widehat{\mathbf{G}})\widehat{\mathbf{b}} + \widehat{\mathbf{d}} \geqslant \mathbf{0}_{4m} \tag{22}$$

where $\mathbf{I}_{4m} \in \Re^{4m \times 4n}$ indicates the identify matrix, $\widehat{\mathbf{C}}$, $\widehat{\mathbf{G}}$ and $\widehat{\mathbf{A}} \in \Re^{4m \times 4m}$ are defined as:

$$\begin{aligned} \widehat{\mathbf{C}} &= \begin{bmatrix} \mathbf{I}_{2m} & \\ & C\mathbf{I}_{2m} \end{bmatrix}, \\ \widehat{\mathbf{G}} &= \begin{bmatrix} \mathbf{0}_{2m\times 2m} & \mathbf{0}_{2m\times m} & \mathbf{0}_{2m\times m} \\ \mathbf{0}_{m\times 2m} & \mathbf{I}_m & \mathbf{0}_{m\times m} \\ \mathbf{0}_{m\times 2m} & \mathbf{0}_{m\times m} & -\mathbf{I}_m \end{bmatrix}, \\ \widehat{\mathbf{A}} &= \begin{bmatrix} \mathbf{0}_{2m\times m} & \mathbf{0}_{2m\times m} & \mathbf{0}_{2m\times 2m} \\ -\boldsymbol{\kappa}_{\text{train}} & \boldsymbol{\kappa}_{\text{train}} & \mathbf{0}_{m\times 2m} \\ \boldsymbol{\kappa}_{\text{train}} & -\boldsymbol{\kappa}_{\text{train}} & \mathbf{0}_{m\times 2m} \end{bmatrix} \end{aligned} \tag{23}$$

and the kernelized vectors $\widehat{\mathbf{a}}$, $\widehat{\mathbf{b}}$, $\widehat{\mathbf{d}}$ and $\widehat{\mathbf{z}} \in \Re^{4m}$ are defined as:

$$\widehat{\mathbf{a}} = \begin{bmatrix} \mathbf{e}_{2m} \\ \mathbf{0}_{2m} \end{bmatrix}, \widehat{\mathbf{b}} = \begin{bmatrix} \mathbf{0}_{2m} \\ \mathbf{e}_{2m} \end{bmatrix}, \widehat{\mathbf{d}} = \begin{bmatrix} \mathbf{0}_{2m} \\ \mathbf{Y}_{\text{train}} \\ -\mathbf{Y}_{\text{train}} \end{bmatrix}, \widehat{z} = \begin{bmatrix} \mathbf{p} \\ \mathbf{q} \\ \boldsymbol{\xi} \\ \boldsymbol{\xi}^* \end{bmatrix} \tag{24}$$

Then, the kernelized X-SVR can be solved with the introduction of the non-negative Lagrange multiplier $\boldsymbol{\varphi} \in \Re^{4m}$. Through the way for solving a quadratic programming (QP) problem, the optimization problem can further be formulated as:

$$\min_{\boldsymbol{\varphi}} : \frac{1}{2}\boldsymbol{\varphi}^{\mathrm{T}}\mathbf{Q}\boldsymbol{\varphi} - \mathbf{m}^{\mathrm{T}}\boldsymbol{\varphi} \tag{25}$$

$$s.t. \boldsymbol{\varphi} \geqslant \mathbf{0}_{4m} \tag{26}$$

where $\mathbf{Q} \in \Re^{4m \times 4m}$ and $\mathbf{m} \in \Re^{4m}$ are defined as:

$$\mathbf{Q} = (\widehat{\mathbf{A}} + \mathbf{I}_{4m})\widehat{\mathbf{C}}^{-1}(\widehat{\mathbf{A}} + \mathbf{I}_{4m})^{\mathrm{T}} + \widehat{\mathbf{G}}\widehat{\mathbf{b}}\widehat{\mathbf{b}}^{\mathrm{T}}\widehat{\mathbf{G}} \tag{27}$$

$$\mathbf{m} = \lambda(\widehat{\mathbf{A}} + \mathbf{I}_{4m})\widehat{\mathbf{C}}^{-1}\widehat{\mathbf{a}} - \varepsilon\widehat{\mathbf{b}} - \widehat{\mathbf{d}} \tag{28}$$

Let $\boldsymbol{\varphi}^*$ be the solution of optimization problems in Eqs. (25) and (26), then the variables $\widehat{\mathbf{z}}$ and δ can be determined as:

$$\widehat{\mathbf{z}} = \widehat{\mathbf{C}}^{-1}\left[(\widehat{\mathbf{A}} + \mathbf{I}_{4m})^{\mathrm{T}}\boldsymbol{\varphi}^* - \lambda\widehat{\mathbf{a}}\right] \tag{29}$$

$$\delta = \widehat{\mathbf{b}}^{\mathrm{T}}\widehat{\mathbf{G}}\boldsymbol{\varphi}^* \tag{30}$$

Then, the nonlinear regression function can be expressed as:

$$\widehat{f}(\mathbf{X}) = (\mathbf{p}-\mathbf{q})^{\mathrm{T}}\kappa(\mathbf{X}) + \widehat{\mathbf{b}}^{\mathrm{T}}\widehat{\mathbf{G}\boldsymbol{\varphi}}^* \tag{31}$$

The coefficient **p** and **q** can be obtained as:

$$\mathbf{p} = \widehat{\mathbf{z}}(1:m) \tag{32}$$

$$\mathbf{q} = \widehat{\mathbf{z}}(m+1:2m) \tag{33}$$

To demonstrate the existence of a globally optimal solution in the X-SVR approach, the convexity of the X-SVR method is required to be proved. Let $\mathbf{v} \in \Re^{4m}$ be an arbitrary non-zero column vector, then,

$$\mathbf{v}^{\mathrm{T}}\mathbf{Q}\mathbf{v} = \left\{ \left[(\widehat{\mathbf{A}} + \mathbf{I}_{4m})^{\mathrm{T}}\mathbf{v} \right]^{\mathrm{T}} \widehat{\mathbf{C}}^{-1} \left[(\widehat{\mathbf{A}} + \mathbf{I}_{4m})^{\mathrm{T}}\mathbf{v} \right] \right\} + \left(\widehat{\mathbf{b}}^{\mathrm{T}}\widehat{\mathbf{G}}\mathbf{v} \right)^2 \geqslant 0 \tag{34}$$

Therefore, the QP problem shown in Eqs. (25) and (26) is convex. As a result, the kernelized X-SVR virtual models can be constructed.

3.2. Automatic Relevance Determination - generalized euler kernel (ARD-GEK)

In the virtual model construction, the selection of kernel function significantly influences the performance of the developed virtual models. Herein, inspired by the successes of the Eulerian polynomials in series expansion, a novel generalized kernel mapping function, namely the Automatic Relevance Determination - Generalized Eulerian kernel (ARD-GEK) is developed, to serve as an additional option for the embedded X-SVR technique.

The global function is Eulerian polynomials, which are defined by the exponential generating function and can be computed by the recurrence,

$$\begin{aligned} E_0(t) &= 1 \\ E_{\lambda}(t) &= E_{\lambda-1}(t)[1 + (\lambda - 1)t] + t(1-t)E'_{\lambda-1}(t), \text{for } \lambda \geqslant 1 \end{aligned} \tag{35}$$

where λ denotes the order of the Eulerian polynomial. In addition to the global function, the Gaussian kernel function is employed as the weighting function to accelerate the convergence speed. Till now, the Generalized Eulerian Kernel (GEK) function can be developed, more specifically,

$$\kappa_{\mathrm{GEK}}\left(\mathbf{X_i}, \mathbf{X_j} \middle| \widehat{\lambda}, \gamma\right) = \frac{\sum_{\lambda=0}^{\hat{\lambda}} E_{\lambda}(\mathbf{X}_i)^{\mathrm{T}} E_{\lambda}(\mathbf{X}_j)}{\exp\left(\gamma \left\| \mathbf{X}_i - \mathbf{X}_j \right\|_2^2\right)} \tag{36}$$

where γ is considered as the length scale. Based on the established GEK, the Automatic Relevance Determination (ARD) strategy [68] is implemented. The aim of this strategy is to adjust the length scale separately for each feature, and eventually, to achieve higher robustness in regression. Thus, the proposed kernel function, ARD-GEK, can be expressed in the form of,

$$\kappa_{\text{ARD-GEK}}\left(\mathbf{X}_i, \mathbf{X}_j \middle| \widehat{\lambda}, \gamma_1, \gamma_2, \ldots, \gamma_{\hat{n}}, \ldots, \gamma_n\right) = \frac{\sum_{\lambda}^{\hat{\lambda}} E_{\lambda}(\mathbf{X}_i)^{\mathrm{T}} E_{\lambda}(\mathbf{X}_j)}{\exp\left(\sum_{\hat{n}=1}^{n} \gamma_{\hat{n}} \left(x_{i,\hat{n}} - x_{j,\hat{n}}\right)^2\right)} \tag{37}$$

where $\gamma_1, \gamma_2, \ldots \gamma_{\hat{n}}, \ldots, \gamma_n \in \Re^+$ denote the characteristics length scales for each predictor. Generally, the proposed ARD-GEK consists of $(n+1)$ hyperparameters in total: the polynomial order $\widehat{\lambda}$ and n-dimensional positive kernel scale parameters $\gamma_1, \gamma_2, \ldots \gamma_{\hat{n}}, \ldots, \gamma_n$. Moreover, it is necessary to highlight that when $\gamma_1 = \gamma_2, \ldots \gamma_{\hat{n}}, \ldots, \gamma_n = \gamma$, the proposed ARD-GEK would degenerate into the predecessor GEK. Accordingly, the robustness of the developed ARD-GEK can be theoretically enhanced compared to the predecessor GEK.

In addition, it is worth mentioning that the proposed GEK satisfies the Mercer Theorem [69–72], which is essentially for implementing the kernel function in support vector theorem-based methods. The property that the proposed GEK is a valid Mercer kernel can be systematically demonstrated by Proposition 1.

Proposition 1. The proposed ARD-GEK expressed in Eq. (37) is a valid Mercer kernel.

Proof. *The proposed ARD-GEK can be expressed as the product of two kernel functions, as shown in Eq. (38)*

$$\kappa_{\text{ARD-GEK}}\left(\mathbf{X}_i, \mathbf{X}_j\right) = \kappa_1\left(\mathbf{X}_i, \mathbf{X}_j\right)\kappa_2\left(\mathbf{X}_i, \mathbf{X}_j\right) \tag{38}$$

in which

$$\kappa_1\left(\mathbf{X}_i, \mathbf{X}_j\right) = \exp\left(-\sum_{\hat{n}=1}^{n} \gamma_{\hat{n}} \left(x_{i,\hat{n}} - x_{j,\hat{n}}\right)^2 \right) \tag{39}$$

$$\kappa_2\left(\mathbf{X}_i, \mathbf{X}_j\right) = \sum_{\lambda=0}^{\hat{\lambda}} E_{\lambda}(\mathbf{X}_i)^{\mathrm{T}} E_{\lambda}(\mathbf{X}_j) \tag{40}$$

Based on [16,73], the multiplication of two valid Mercer kernels is also a valid kernel function. As $\kappa_1(\mathbf{X}_i, \mathbf{X}_j)$ is the multiplication of the Gaussian kernel that satisfies the Mercer Theorem, $\kappa_{\text{ARD-GEK}}$ can be proved as satisfying the Mercer Theorem by proofing that $\kappa_2(\mathbf{X}_i, \mathbf{X}_j)$ satisfies the Mercer Theorem.

Given an arbitrary squared integrable function $g(x)$ defined as $g: \Re^n \to \Re$ and assuming each element in $\mathbf{X}_i$ and $\mathbf{X}_j$ is independent with each other, then

$$\begin{aligned}
&\iint \kappa_2(\mathbf{X}_i, \mathbf{X}_j) g(\mathbf{X}_i)^{\mathrm{T}} g(\mathbf{X}_j) d\mathbf{X}_i d\mathbf{X}_j \\
&= \iint \sum_{\lambda=0}^{\hat{\lambda}} E_\lambda(\mathbf{X}_i)^{\mathrm{T}} E_\lambda(\mathbf{X}_j) g(\mathbf{X}_i)^{\mathrm{T}} g(\mathbf{X}_j) d\mathbf{X}_i d\mathbf{X}_j \\
&= \sum_{\lambda=0}^{\hat{\lambda}} \iint E_\lambda(\mathbf{X}_i)^{\mathrm{T}} E_\lambda(\mathbf{X}_j) g(\mathbf{X}_i)^{\mathrm{T}} g(\mathbf{X}_j) d\mathbf{X}_i d\mathbf{X}_j \\
&= \sum_{\lambda=0}^{\hat{\lambda}} \left[\int E_\lambda(\mathbf{X}_i)^{\mathrm{T}} g(\mathbf{X}_i) d\mathbf{X}_i \int E_\lambda(\mathbf{X}_j)^{\mathrm{T}} g(\mathbf{X}_j) d\mathbf{X}_j \right] \\
&= \sum_{\lambda=0}^{\hat{\lambda}} \left\{ \left[\int E_\lambda(\mathbf{X}_i)^{\mathrm{T}} g(\mathbf{X}_i) d X_i \right] \left[\int E_\lambda(\mathbf{X}_j)^{\mathrm{T}} g(\mathbf{X}_j) d\mathbf{X}_j \right] \right\} \geqslant 0
\end{aligned} \tag{41}$$

Therefore, $\kappa_2(\mathbf{X}_i, \mathbf{X}_j)$ is a valid Mercer kernel and $\kappa_{\text{ARD-GEK}}(\mathbf{X}_i, \mathbf{X}_j)$ is an admissible Mercer kernel function.

This concludes the proof.□.

Since the developed ARD-GEK is a mixed kernel function that combines a local kernel $\kappa_1(\mathbf{X}_i, \mathbf{X}_j)$ (i.e., ARD-Gaussian kernel) and a global kernel $\kappa_2(\mathbf{X}_i, \mathbf{X}_j)$ (i.e., GEK), the developed ARD-GEK is considered as a multiple kernel learning algorithm using fixed rules and facilitating a separating length scale for each predictor. Theoretically, the introduction of the local Gaussian kernel improves the convergence speed, and the adopted ARD method enhances the robustness of the GEK. Convincedly, the proposed ARD-GEK serves as an additional option of kernel function to the embedded X-SVR method for solving complex engineering problems.

3.3. Cross-validation (CV) and hyperparameter tunning

To ensure the accuracy of prediction by developed virtual models and avoid overfitting, the cross-validation (CV) strategy is employed within the X-SVR method [16]. The measurement of training error is measured by the 5-fold CV error, denoted as $Err_{5\text{cv}}$, that is calculated as

$$Err_{5\text{cv}} = \frac{1}{5} \sum_{\vartheta=1}^{5} err_\vartheta \tag{42}$$

where err_ϑ indicates mean squared error (*MSE*) between the true function value ($\mathbf{Y}_\vartheta \in \Re^{m_\vartheta}$) and the predicted value by X-SVR ($\widehat{f}_\vartheta(\mathbf{X}_\vartheta) \in \Re^{m_\vartheta}$) in the ϑth fold. Specifically, err_ϑ is calculated as

$$err_\vartheta = \frac{1}{m_\vartheta} \sum_{\varpi=1}^{m_\vartheta} \left[Y_{\vartheta,\varpi} - \widehat{f}(\mathbf{X}_{\vartheta,\varpi}) \right]^2, \text{ for } \vartheta = 1, 2, \cdots, 5 \tag{43}$$

where m_ϑ indicates the number of training samples in the ϑth fold; $Y_{\vartheta,m}$ represents the ϖth component in $\mathbf{Y}_\vartheta$; $\mathbf{X}_\vartheta \in \Re^{m_\vartheta \times n}$ collects the training inputs of the ϑth fold; $\mathbf{X}_{\vartheta,\varpi} \in \Re^n$ indicates the ϖth component in $\mathbf{X}_\vartheta$ and $\widehat{f}(\mathbf{X}_{\vartheta,\varpi})$ denotes the model prediction for $\mathbf{X}_{\vartheta,\varpi}$.

The accuracy of the established virtual models depends on hyperparameters. The X-SVR method using ARD-GEK contains $(n + 4)$ hyperparameters, including a regularization parameter λ, penalty parameter C, insensitive tube width ε, the polynomial order $\widehat{\lambda}$ and n-dimensional positive kernel parameters $\gamma_1, \gamma_2, \cdots, \gamma_n$. When the kernel mapping strategy is utilized, the dimension of the input n equals the size of the training sample m. In many cases, the training sample size is generally large, which consequently leads to a significant number of hyperparameters. Manual searching is infeasible for humans due to such high dimensionality. In addition, the grid searching method would also be stuck due to the dimensionality curse. To effectively tune hyperparameters, Bayesian optimization is embedded

Table 1
Searching ranges for hyperparameters.

Hyperparameter	Searching range
λ	[1e-5, 1]
C	[1e3, 1e6]
ε	[1e-7, 1e-4]
$\widehat{\lambda}$	[0, 8]
$\gamma_1, \gamma_2, \cdots, \gamma_n$	[0.1, 50]

into the X-SVR method for minimizing Err_{5cv}, in which both Gaussian and non-Gaussian processes can be used [73,74]. Since hyperparameter tunning by Bayesian optimization is the secondary problem in this research, the detailed algorithm can be referred to in the references [75–77]. The searching ranges of hyperparameters in the developed ARD-GEK are summarized in Table 1.

By virtue of the X-SVR approach, the implicit and sophisticated relationships between system parameters and the structural responses can be translated into explicit differentiable equations. Therefore, instead of solving the complicated constitutive equations, the problem is formulated into a series of constrained optimization programming on the virtual models. Once the virtual models are constructed, the following estimations of structural outputs are independent to the structural mesh and complex governing equations of the physical models. Via the solid mathematical support, this X-SVR approach significantly relief the pressure from computational efficiency in solving the original constitutive relationships. Accordingly, the adequate statistical information and structural reliability of concerned responses in EMMs can be estimated efficiently based on a proposed virtual model-aided framework, i.e., a novel metamodel-based MCS, introduced in Section 4.

4. Virtual model-aided structural reliability analysis for 3D EMMs

To efficiently and effectively conduct reliability analysis of bandgap characteristics for 3D EMMs, a novel virtual model-aided framework is developed. This novel framework consists of two main parts including *Part I: Virtual model construction* and *Part II: Structural reliability assessment*, intuitively demonstrated in Fig. 2.

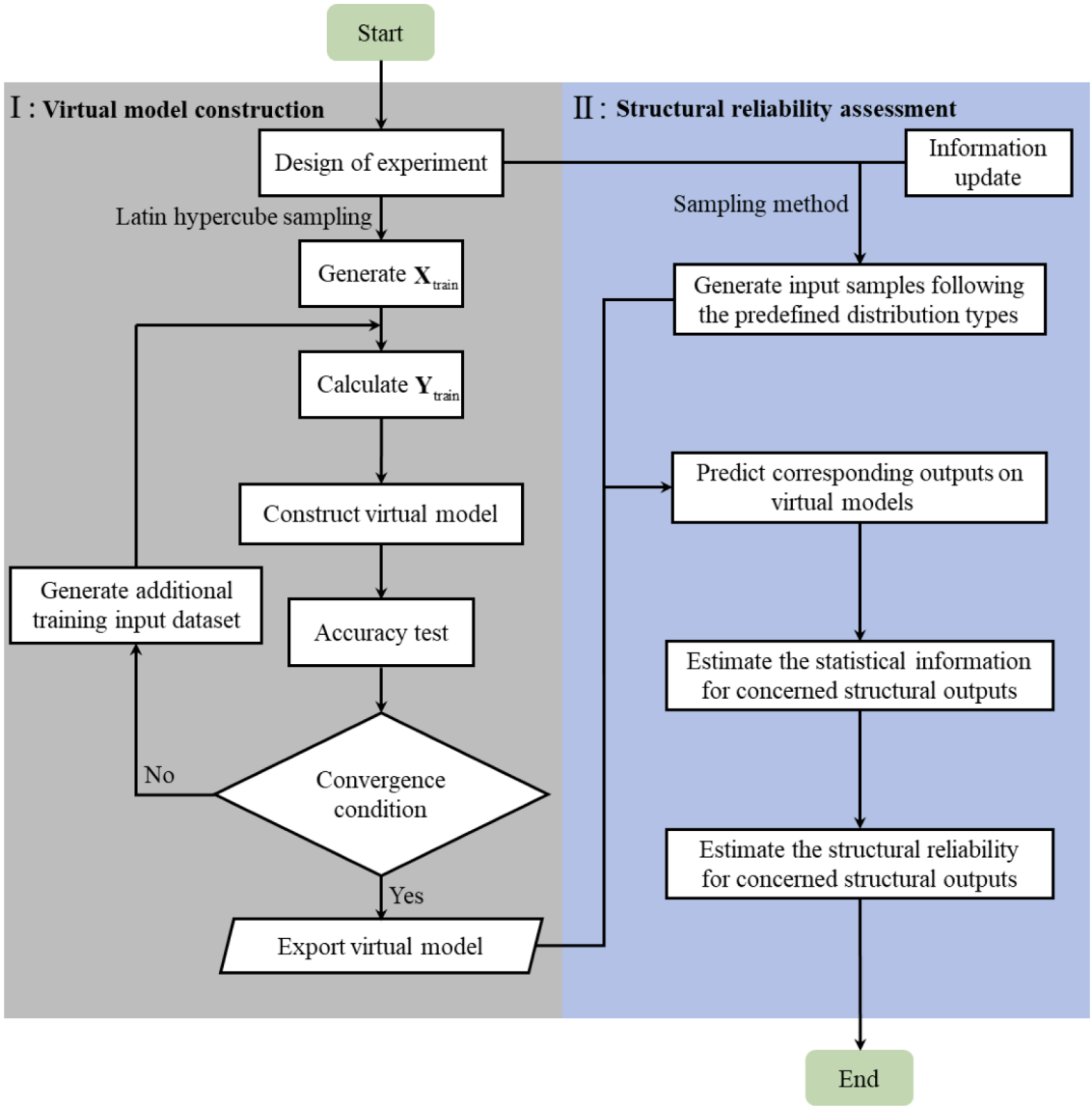

Fig. 2. Virtual model-aided framework for structural reliability assessment.

In *Part I*, the main purpose is to establish effective virtual models, which reveal the underpinned constitutive relationships between the system parameters and concerned structural responses (i.e., f_s and f_c). The virtual model construction is started with the design of experiment to clarify the physical problem, concerned structural responses and statistical information of uncertainties, including means, standard deviations and distribution types. Generally, the proposed framework supports multiple sources of datasets, including information and communication techniques, numerical simulation, experiments, and historical records [23]. However, herein, the main source of the training datasets is generated through numerical simulation. The training input dataset $\mathbf{X}_{\text{train}}$, containing specific realizations of the system uncertainties $\boldsymbol{\xi}^{\text{R}}$, can be generated through sampling methods, such as Latin hypercube sampling (LHS), Quasi-MCS (Sobol sequence or Halton sequence), etc. [78,79]. In this work, the training input samples are generated by a widely used sampling method, i.e., LHS, which can provide full coverage of the range for each variable [80–82]. By implementing MCS on the FEM models, training dataset output $\mathbf{Y}_{\text{train}}$ is obtained, which are specific realization for concerned random bandgap properties (i.e., f_s^{R} or f_c^{R}). In addition to the support of multiple data sources, the high compatibility of the proposed framework can be further highlighted, since various machine learning techniques, data processing techniques (e.g., dimension reduction, normalization, sampling, and noise discard strategies), and postprocessing techniques can be easily integrated into the proposed framework [83–85].

In this research work, the X-SVR method is employed to develop virtual models, revealing the underpinned relationships between structural parameters and concerned structural responses. The embedded X-SVR method can be formulated into a QP problem, which means that the global optimum solution can be obtained by any QP or convex solvers. To avoid overfitting in the constructed virtual models, a 5-fold CV is adopted in the X-SVR method. Furthermore, to effectively and efficiently tune hyperparameters, Bayesian optimization is employed, which can solve the minimum objective function with fewer iterations compared with the traditional method, such as grid searching. In this work, the maximum iteration for Bayesian optimization is set as 50.

To establish effective virtual models revealing the relationship between structural parameters and outputs, a convergence study is conducted to determine the size of training samples. In addition, for each specific training sample size, virtual models are constructed repeatedly 20 times to assess computational stability and accuracy. To further improve the robustness of the embedded virtual modelling technique, a novel generalized kernel function is proposed. The developed kernel function integrates the Automatic Relevance Determination (ARD) strategy and Generalized Eulerian kernel (GEK), namely ARD-GEK to serve as an additional option for kernel mapping in applications. It is worth noting that when the local widths share the same value, the developed ARD-GEK can degenerate into the original GEK.

Afterwards, *Part II* is executed for assessing the reliability of bandgap characteristics for 3D EMMs. In this paper, datasets for system uncertainties are established by utilizing sampling methods. With the aid of the explicit formulations of the virtual models, datasets with a sufficient amount of sampling points can be obtained in an efficient manner. Afterwards, adequate statistical information, such as means, standard deviations, PDFs, and CDFs can be estimated for concerned structural responses with the implementation of MCS. The estimated structural reliability concerning f_s^{R} for an EMM by the proposed virtual model-aided framework is presented as follows:

$$P_r = Pr\left(f_s^{\text{R}} \leqslant f_s^*\right) \approx Pr\left(\widehat{f}_s \leqslant f_s^*\right) = \int_{-\infty}^{f_s^*} f_{\widehat{f}_s}^{\text{D}}(x)dx \approx \frac{1}{N}\sum_{\varsigma=1}^{N} \ddot{\text{I}}\left(\widehat{f}_s^{\varsigma} \leqslant f_s^*\right) \tag{44}$$

in which f_s^* represents the capacity of the system for f_s^{R}; N denotes the number of sampling points; $\ddot{\text{I}}[\bullet]$ denotes an indicate function which equals 1 if $[\bullet]$ is true and 0 if $[\bullet]$ is false; $\widehat{f}_s^{\varsigma}$ denotes the predicted response for f_s by the constructed virtual model at the ςth realization for random variables. It is worth mentioning that the estimated structural reliability with the aid of the virtual model is not equivalent to the theoretical value in Eq. (13). Errors can be induced from three sources, including the error in FEM physical models, the errors between FEM models and virtual models, and statistical errors resulting from sampling methods. Specifically, it can be noted from Eq. (44) that both the sampling size and realizations generated by sampling methods can contribute to errors in the failure probability estimation.

As a partially non-intrusive method, once the virtual model has been established, the subsequent virtual model-aided EMM reliability analysis can avoid the computationally expensive calculation on the FEM model. Besides, it is worth mentioning that the virtual model training process is independent of distribution types for random inputs. After the virtual model is developed, the statistical information and structural reliability can be estimated for concerned structural responses based on the newly generated samples of random variables following updated distribution types. However, one limitation of the information update feature is that additional training datasets may be required for developing effective virtual models if the random structural parameters vary over larger ranges. Further analysis, such as design optimization, sensitivity analysis, and structural health monitoring can be conducted based on the established virtual models with ease.

Generally, the advantages of the proposed framework can be summarized as follows:

(1) A systematic reliability analysis framework is proposed to quantitatively investigate material and geometrical uncertainties separately or simultaneously on structural reliability for EMMs.
(2) A virtual modelling technique is embedded into the framework to reveal the underpinned and implicit constitutive relationships between structural parameters and concerned structural responses for 3D EMMs based on a limited number of datasets. The established virtual model can be formulated as a continuous explicit mathematical equation through the X-SVR technique.
(3) Calculation on virtual models can bypass complicated tasks in original physical models, such as domain discretization, meshing, assembling structural matrix and evaluating sophisticated governing relationships within the framework of the FEM method.

(4) By integrating the established virtual models with sampling-based methods, sufficient statistical information, including means, standard deviations, PDFs, CDFs, and structural reliability can be estimated in an efficient and effective manner.
(5) Once virtual models are developed, information update is an inherent feature. It facilitates the calculation of the concerned structural response on the established virtual model following any updated statistical information of the system inputs without re-running the relatively computationally exhaustive physical model and subsequently benefits in updating the structural reliability.
(6) The proposed framework possesses high compatibility, which can be integrated with various sources of datasets, machine learning methods, and data processing techniques.

5. Numerical investigations

In the numerical investigation, the effectiveness and computational efficiency of the proposed virtual model-aided reliability framework for a lattice-based 3D EMM by considering both material and geometrical uncertainties are demonstrated. For 3D EMMs, they usually possess more complicated constitutive relationships between structural parameters and concerned bandgap characteristics compared with 1D and 2D EMMs [43–46]. To substitute the sophisticated underpinned physical relationship in a 3D EMM with a virtual model, the embedded virtual modelling technique is required to demonstrate high robustness. In addition, since the deterministic dispersion analysis for 3D EMMs already requires a large computational cost, to maintain the high applicability of the proposed framework, the employed virtual modelling technique is requested to illustrate high convergence speed in virtual model construction. To fulfil this task, the recently developed X-SVR method is adopted. The convergence speed, stability, robustness, and accuracy of the method are investigated thoroughly in three numerical investigation cases. In Cases A and B, material and geometrical uncertainties are considered separately in unit cells, in which each case involves three random variables. Then, the structural reliability analysis is implemented in Case C by considering both material and geometrical uncertainties simultaneously for the 3D EMM, involving six random variables. In addition, other popular machine learning methods, e.g., the traditional support vector regression (SVR) and neural network (NN), are also adopted in comparisons. All simulations are run in MATLAB. Statistics and machine learning toolbox is used to train virtual models by SVR and NN techniques, in which default settings are employed [86]. Specifically, when implementing SVR, the default Gaussian kernel is used. In NN models, the number of outputs in the first three fully connected layers are 10, 5, and 10, respectively. Before investigating structural reliability, a deterministic analysis is conducted, illustrating the detailed procedure to evaluate the concerned structural responses by FEM in a single realization.

5.1. The 3D EMM design and its deterministic bandgap analysis

The numerical investigation is implemented on a lattice-based 3D EMM, the structural layouts are depicted in Fig. 3(a) and (b). Lattice-based EMMs have attracted significant attention due to their high stiffness-to-density ratio and excellent lattice symmetry, which have great potential to be implemented for a wide range of real-life engineering applications, including vibration control,

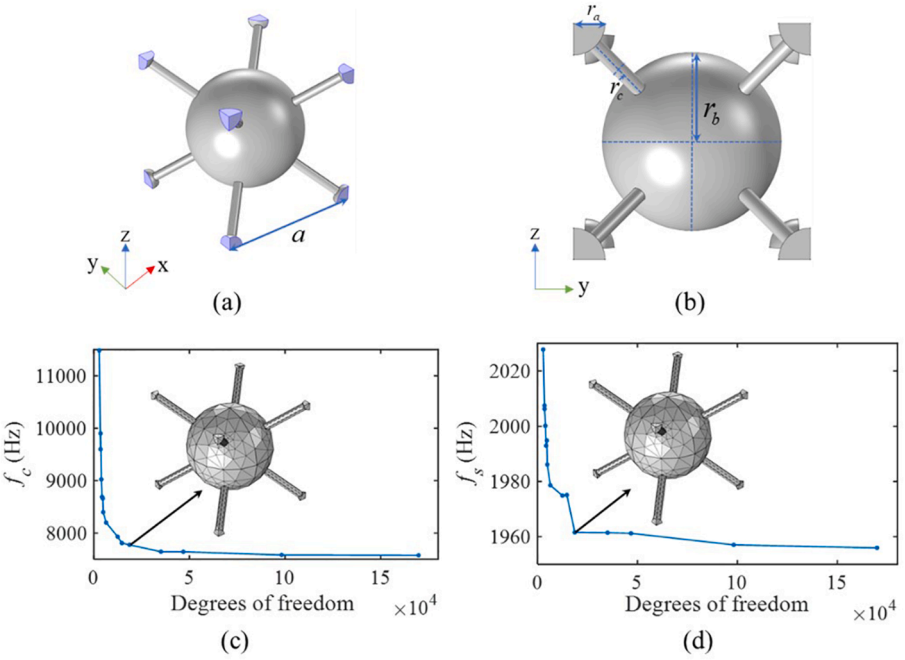

Fig. 3. (a) Structural layout of the 3D EMM unit cell in a (a) 3D view, (b) 2D view; convergence study for (c) f_s and (d) f_c.

vibration suppression, and noise reduction [87].

The unit cell is characterized by four geometrical parameters including the unit cell size a, cornered sphere radius r_a, centered sphere radius r_b, and connected cylinder radius r_c. In the numerical simulations, the material with Young's modulus $E = 2$ GPa, density $\rho = 1150\ \mathrm{kg/m^3}$, and Poisson's ratio $\upsilon = 0.4$ [11] is endowed to the EMMs. Bloch-Floquet boundary conditions [11] are applied on the boundary surfaces of the unit cells colored in blue as shown in Fig. 3(a). According to the convergence study in Fig. 3(c) and (d), obvious convergence trends are observed when the DoF reaches to 18645. The correspondingly adopted mesh with 3176 tetrahedra elements is illustrated. Based on the governing equation illustrated in Eq. (6), the deterministic bandgap solution of the EMM with a = 30 mm, r_a=2 mm, r_b=12 mm, and $r_c = 1$ mm along the **k**-path of the First Brillouin zone is evaluated and presented in Fig. 4 [51]. The adopted **k**-path is Γ - X - M - Γ - R - X|M - R, where Γ represents the center of the Brillouin zone, M denotes the center of the edge, R demonstrates a corner point, and X indicates the center of a face, respectively.

The concerned 1st bandgap is described by two variables including the starting frequency (f_s) and the cut-off frequency (f_c) labelled in Fig. 4. These two quantities are the concerned structural responses in the subsequent structural reliability analysis.

5.2. Case A: material uncertainty in the unit cell

In the structural reliability analysis considering material uncertainties, the material properties for the 3D EMM unit cell are considered as mutually independent random variables following uniform distributions within the ranges of $[1.90e9,\ 2.10e9]$Pa for E, $[1093.25,\ 1207.50]\mathrm{kg/m^3}$ for ρ, and $[0.38, 0.42]$ for υ, respectively. Training input dataset is generated by LHS and corresponding concerned structural outputs, i.e., f_s and f_c are computed by FEM to obtain the training output dataset. Besides the X-SVR method, the other two popular machine learning techniques, e.g., the traditional support vector regression (SVR) and neural network (NN), are also implemented in comparison, regarding computational convergence, accuracy, and stability. The brute FEM-based MCS with 2e3 iterations is conducted as the benchmark. The estimation metrics listed in Table 2 are employed to quantitatively assess the computational accuracy of the constructed virtual models.

To establish effective virtual models bridging the underpinned relationship between material properties and the concerned structural responses, the convergence study is conducted on the virtual models with adjusted training sample sizes (i.e., training sample size = 10, 25, 50, 100, 150, and 200). R^2 and *RMSE* are estimated for the established virtual models by the three machine learning techniques. Furthermore, a mutually independent calculation is repeated 20 times to test the computational stability. The results are summarized in the boxplots shown in Figs. 5–8. It is worth mentioning that FEM on MCS, X-SVR on MCS, SVR on MCS, and NN on MCS are simplified as FEM, X-SVR, SVR, and NN in the following figures and tables.

Based on the results in Figs. 5–8, obvious convergence trends are noticed in R^2 and *RMSE* for the established virtual models by these three machine learning methods. The thickness of the box indicates the dispersion of the results, and the red '+' marker represents the outliers. It is noticed that the virtual models constructed by the embedded X-SVR approach share faster convergence speed and higher computational stability, with the thinnest boxes and little outliers. Moreover, scatter plots are demonstrated when the training sample size is 100, intuitively illustrating the dispersion of the estimated results in reference to the brute MCS results. Based on the plots, it is found that the estimations by the X-SVR method possess less dispersion compared with the results by SVR and NN techniques. Accordingly, the X-SVR method surpasses the traditional SVR method and NN in the virtual model construction for revealing the relationships between material properties and concerned outputs, in terms of convergence speed, computational accuracy, and stability.

When the training datasets reach 100, effective virtual models with extraordinary performance in computational accuracy and stability can be established by the X-SVR approach. In the subsequent calculation, the evaluation of the complicated constitutive relationship between the system parameters and the concerned structural responses is no longer required. The concerned structural outputs can be estimated by the established explicit formations, which significantly relieve the pressure from computational efficiency.

Subsequently, the PDFs and scatter plots of f_s and f_c are estimated. The associated computational results are shown in Figs. 9 and 10.

From Figs. 9 and 10, the PDFs of f_s and f_c are successfully estimated by the established X-SVR virtual models learnt from 100 training samples. High overlapping can be observed between the estimations by the X-SVR and the exhaustive MCS method. The superior performance of the X-SVR technique in virtual model construction is further demonstrated by the least dispersion in scatter

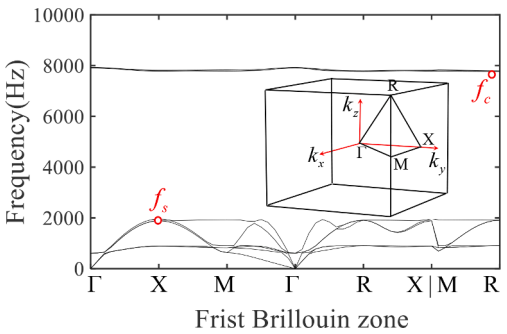

Fig. 4. Band structure along the **k**-path in the First Brillouin zone of the EMM.

Table 2
Estimation metrics.

Estimation metric	Formulation
R-squared (R^2)	$R^2 = 1 - \frac{\sum_N (Y - \widehat{Y})^2}{\sum_N (Y - \overline{Y})^2}$
Root Mean Square Error (*RMSE*)	$RMSE = \sqrt{\frac{\sum_N (Y - \widehat{Y})^2}{N}}$
Relative Error (*RE*)	$RE = \frac{Y - \widehat{Y}}{Y} \times 100\%$

*where Y, $\widehat{Y}$, and $\overline{Y}$ denote the FEM-based MCS results, virtual models estimation, and the mean of the FEM-based MCS results respectively; N represents the number of samples.

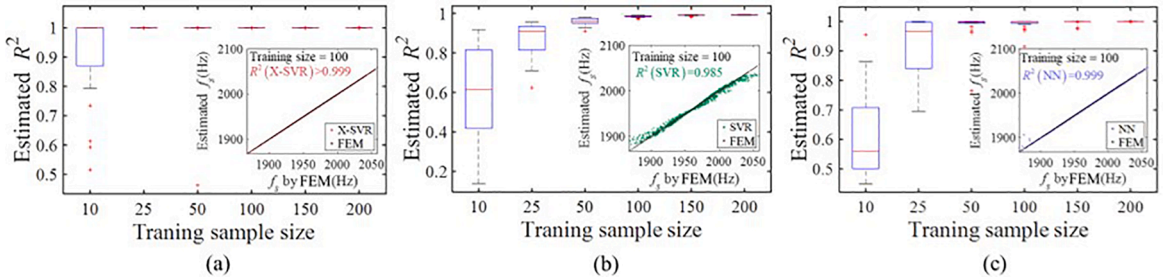

Fig. 5. Estimated R^2 of the virtual models for f_s by (a) X-SVR, (b) SVR, and (c) NN.

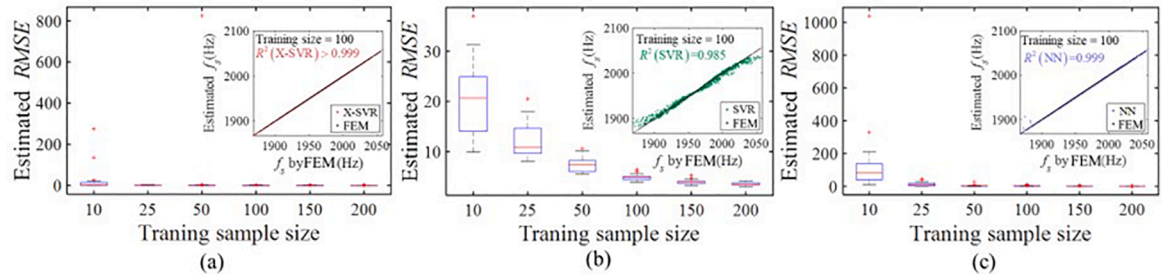

Fig. 6. Estimated *RMSE* of virtual models for f_s by (a) X-SVR, (b) SVR, and (c) NN.

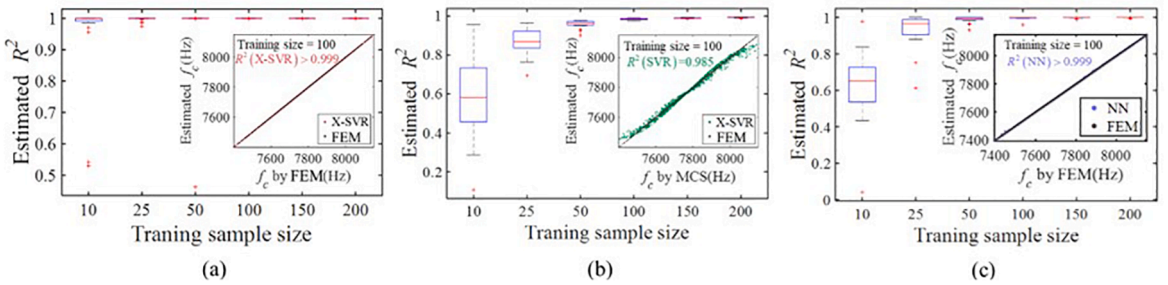

Fig. 7. Estimated R^2 of the virtual models for f_c by (a) X-SVR, (b) SVR, and (c) NN.

plots, in comparison to the traditional SVR and NN approaches. To further highlight the high computational accuracy of the developed virtual models, 7 concerned statistical information (i.e., μ, $\mu \pm \sigma$, $\mu \pm 2\sigma$, and $\mu \pm 3\sigma$) of f_s and f_c are estimated and shown in Tables 3 and 4, respectively. The brute FEM-based MCS results are presented as the reference.

It is clearly shown in Tables 3 and 4 that the statistical information of both f_s and f_c can be estimated accurately by the X-SVR virtual models. The maximum absolute value of *RE* in estimating f_s is 7.66e-55 %, which is excessively lower than 0.26 % and 0.045 % by SVR

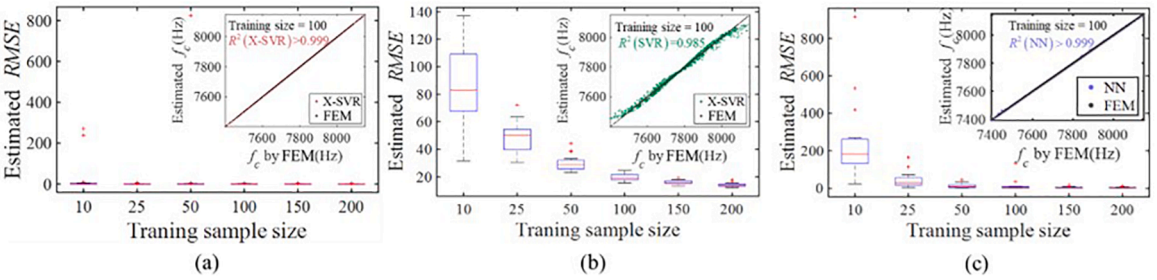

Fig. 8. Estimated *RMSE* of the virtual models for f_c by (a) X-SVR, (b) SVR, and (c) NN.

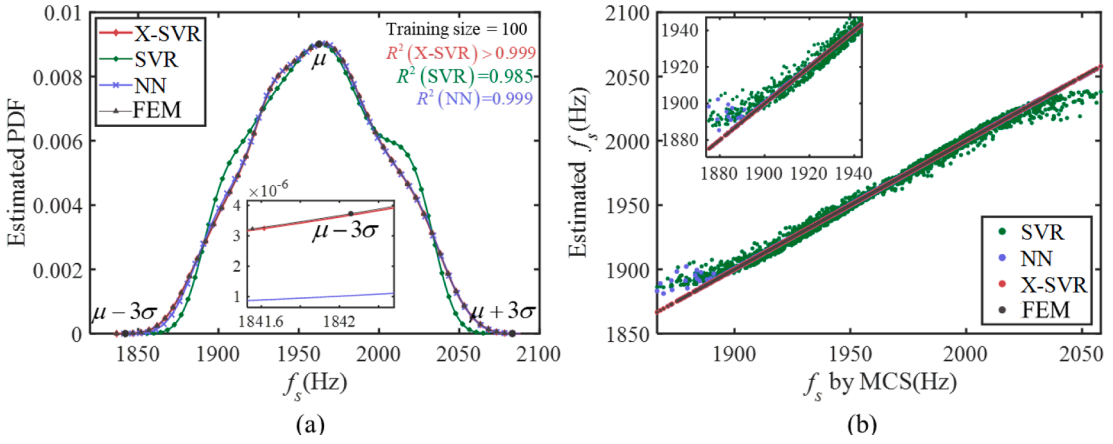

Fig. 9. Estimated (a) PDFs and (b) the scatter plot of f_s for the EMM involving material uncertainties.

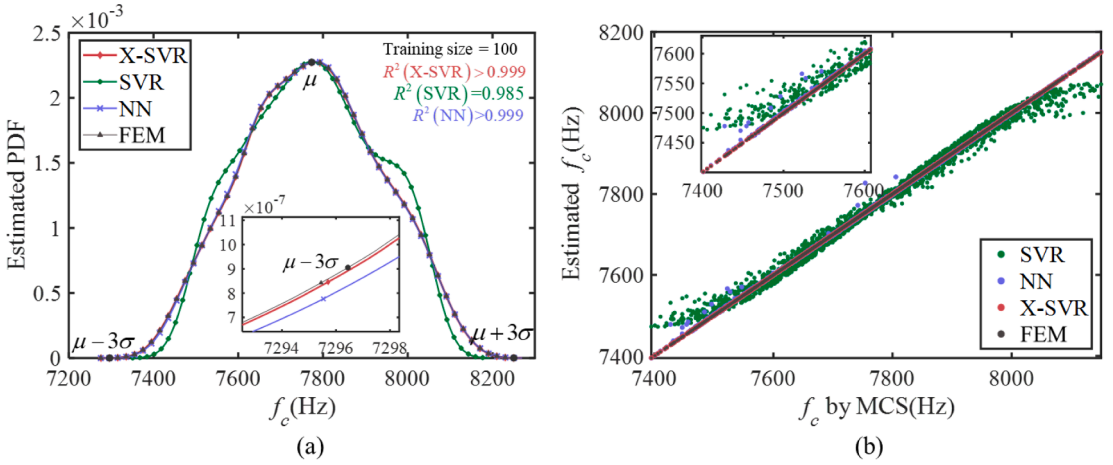

Fig. 10. Estimated (a) PDFs and (b) the scatter plot of f_c for the EMM involving material uncertainties.

and NN methods, respectively. Meanwhile, an extremely narrow range of *REs* between -1.94e-4 and 4.65e-4 % is noted in estimating the local statistical information for f_c by the X-SVR virtual model. The corresponding ranges of *REs* by the SVR and NN methods are [-0.25, 0.27]% and [-0.015, 0.021]%, respectively, which are significantly larger in contrast to the results by the X-SVR approach.

Then, statistical tests are conducted to demonstrate the capability of the proposed method to estimate means and variances for f_s and f_c. Different samples are generated when MCS sample sizes are set as 5, 10, 25, 50, 75, 100, 125, 350, 500, 750, and 1000 respectively. The convergence plots of the estimated means and variances for f_s and f_c are shown in Figs. 11 and 12 respectively.

It can be seen from Figs. 11 and 12 that obvious convergence trends are observed in the estimated statistical information by the two approaches when the MCS sample size reaches 1000. Moreover, the *REs* of estimated means for f_s and f_c at the MCS sample size of 1000 are only 2.59e-2 % and 2.36e-2 %, respectively.

Table 3
The estimated statistical information of f_s when sampling size is 2e3 iterations. (Unit: Hz).

Location	FEM	X-SVR	*RE* (%)	SVR	*RE* (%)	NN	*RE* (%)
$\mu-3\sigma$	1842.07087	1842.20723	7.66e-5	1846.90013	0.26	1842.89611	0.045
$\mu-2\sigma$	1882.23236	1882.23364	6.80e-5	1885.39761	0.17	1882.82684	0.032
$\mu-\sigma$	1922.39384	1922.39499	5.98e-5	1923.89449	0.078	1922.75758	0.019
μ	1962.55532	1962.55634	5.19e-5	1962.39167	-8.33e-3	1962.68832	0.0068
$\mu+\sigma$	2002.71681	2002.71770	4.44e-5	2000.88885	-0.091	2002.61906	-0.0049
$\mu+2\sigma$	2042.87829	2042.87905	3.71e-5	2039.38603	-0.17	2042.54980	-0.016
$\mu+3\sigma$	2083.03977	2083.04040	3.01e-5	2077.88321	-0.25	2082.48054	-0.027
R^2	N/A	>0.99999	N/A	0.98511	N/A	0.99892	N/A
RMSE	N/A	0.027567	N/A	4.73194	N/A	1.31555	N/A

Table 4
The estimated statistical information of f_c when sampling size is 2e3 iterations. (Unit: Hz).

Location	FEM	X-SVR	*RE* (%)	SVR	*RE* (%)	NN	*RE* (%)
$\mu-3\sigma$	7296.54502	7296.57894	4.65e-4	7316.30688	0.27	7298.09748	0.021
$\mu-2\sigma$	7455.27999	7455.53601	3.43e-4	7468.50211	0.17	7456.61215	0.015
$\mu-\sigma$	7614.51098	7614.52827	2.27e-4	7620.69735	0.081	7615.12681	0.0081
μ	7773.49397	7773.50294	1.15e-4	7772.89256	-0.0077	7773.64148	0.0019
$\mu+\sigma$	7932.47695	7932.47760	8.22e-6	7925.08782	-0.093	7932.15614	-0.0040
$\mu+2\sigma$	8091.45993	8091.45226	-9.47e-5	8077.28306	-0.18	8090.67081	-0.0098
$\mu+3\sigma$	8250.44291	8250.42693	-1.94e-4	8229.47829	-0.25	8249.18547	-0.015
R^2	N/A	>0.99999	N/A	0.98496	N/A	0.99960	N/A
RMSE	N/A	0.12280	N/A	18.80417	N/A	3.17915	N/A

Then, structural reliability is estimated when both f_s^* and f_c^* are set as the values corresponding to μ, $\mu\pm\sigma$, $\mu\pm2\sigma$, and $\mu\pm3\sigma$, respectively. The corresponding values are summarized in Tables 3 and 4. It is worth mentioning that the widely used MCS on physical models is adopted as the benchmark to demonstrate the computational accuracy of the virtual model-aided framework [88–90]. Then, the estimated structural reliability is compared based on the estimation metrics *RE* when the sampling sizes are 2e3 iterations to further highlight the high computational accuracy. By virtue of developed virtual models with high computational efficiency, structural reliability for the EMM is estimated when sampling sizes reach 1e5 iterations. The computational results are summarized in Tables 5 and 6 for the concerned structural responses f_s and f_c, respectively.

From Tables 5 and 6, it is found the structural reliability for f_s and f_c are accurately estimated by the X-SVR approach compared with the MCS benchmark. The largest deviations are found at $\Pr(f_s\leq1842.07087)$ and $\Pr(f_c\leq7296.54502)$ with *RE*s of -1.34 % and 0.71 % respectively. Furthermore, it is worth mentioning that the accuracy for the estimation of structural reliability depends on f_s^* and f_c^*. Quantification of the structural reliability relating to rare events is critical to avoid structural failure in real-life applications. The X-SVR algorithm still possesses outstanding performance to estimate structural reliability. Hence, by only utilizing 100 training samples, it is well demonstrated that the embedded X-SVR approach is capable of generating effective virtual models, showing extraordinary computational accuracy to estimate structural reliability. Moreover, the high computational efficiency of the X-SVR method is highlighted with more statistical data. All computations were carried out on a workstation with Intel(R) Core(TM) Gold 5215 CPU @ 2.54GH 2.49 GHz. To estimate the structural reliability by the virtual model-aided framework, the main computational resources were

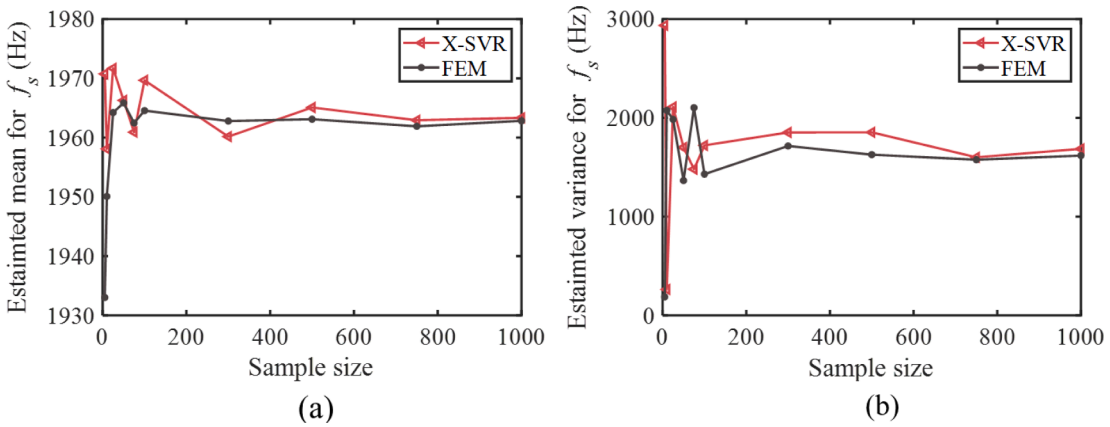

Fig. 11. Convergence plots of the estimated (a) mean and (b) variance for f_s.

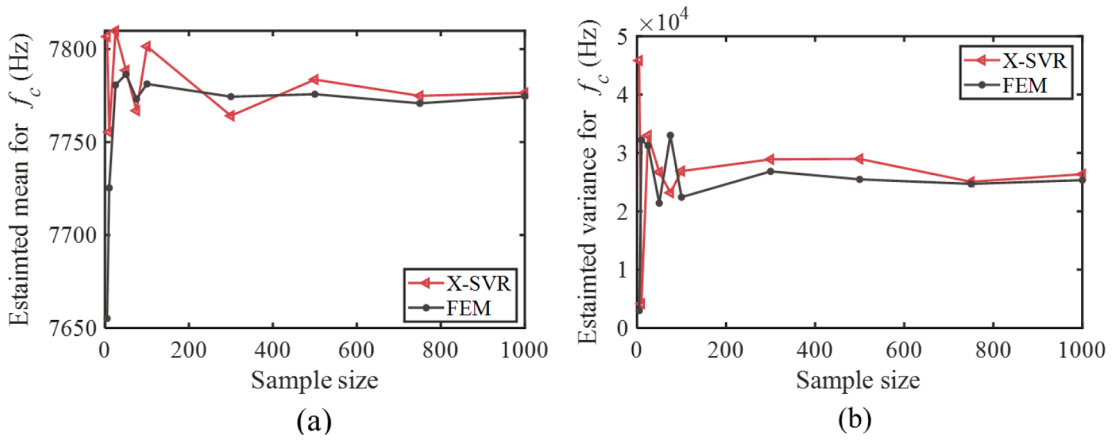

Fig. 12. Convergence plots of the estimated (a) mean and (b) variance for f_c.

Table 5
Estimated structural reliability of f_s.

f_s^* (Hz)	$Pr(f_s \leqslant f_s^*)$			
	FEM (2e3 iterations)	X-SVR (2e3 iterations)	*RE* (%)	X-SVR (1e5 iterations)
1842.07087	1.214658e-5	1.1984e-5	-1.34	<1e-20
1882.23236	0.019970	0.019945	-0.13	0.016807
1922.39384	0.17866	0.17877	6.16e-2	0.17913
1962.55532	0.50360	0.50357	-5.96e-3	0.50910
2002.71681	0.81577	0.81568	-1.10e-2	0.82542
2042.87829	0.97920	0.97926	6.13e-3	0.98055
2083.03977	0.99998	0.99998	4.70e-6	>0.99999

Table 6
Estimated structural reliability of f_c.

f_c^* (Hz)	$Pr(f_c \leqslant f_c^*)$			
	FEM (2e3 iterations)	X-SVR (2e3 iterations)	*RE* (%)	X-SVR (1e5 iterations)
7296.54502	1.16268e-5	1.1709e-5	0.71	<1e-20
7455.27999	0.019893	0.019902	4.52e-2	0.017306
7614.51098	0.17880	0.17875	-2.80e-2	0.18014
7773.49397	0.50381	0.50375	-1.19e-2	0.51068
7932.47695	0.81557	0.81558	1.23e-3	0.82649
8091.45993	0.97922	0.97928	6.13e-3	0.98084
8250.44291	0.99998	0.99998	9.45e-6	>0.99999

consumed by the dataset establishment. By utilizing FEM, it took approximately 9.17 h to construct datasets with 100 sampling points. The subsequent estimation of structural responses with 1e5 iterations required less than 1 s. Alternatively, under the same computational environment, the exhaustive MCS method with 2e3 iterations took 183.34 h in total, which was significantly larger than the consumed resources to estimate structural reliability by the metamodel-based approach with 1e5 iterations.

Subsequently, the capability of the developed framework to estimate statistical information for concerned structural responses following multiple distribution types is demonstrated. By generating new samples following various distribution types, concerned structural responses, statistical information, and structural reliability are estimated with the aid of the developed virtual models. In the numerical example, the updated statistical information of the system uncertainties is summarized in Table 7.

Table 7
Updated statistical information of the material properties.

Random variable	Distribution type	μ	σ
E(GPa)	Extreme value	2.00	0.013
ρ(kg/m^3)	Lognormal	1150	11.36
υ	Normal	0.4	0.004

Since extreme values for material properties are impractical in real-life scenarios, sample points are truncated at the ranges of [1.92e9, 2.02e9] Pa for E, [1.11e3, 1.19e3] kg/m^3 for ρ, and [3.88e-1, 4.16e-1] for υ. Through the developed virtual models, the statistical moments of f_s and f_c are estimated. The brute FEM-based MCS with 2e3 iterations is conducted as the benchmark for assessing computational accuracy. The computational results are summarized in Table 8.

From Table 8, the accuracy in estimating statistical moments by the X-SVR approach is well demonstrated by referring to the highly matched μ and σ for f_s and f_c in contrast to the MCS results. Furthermore, the effectiveness of the virtual model is further highlighted by referencing to the R^2-values nearly 1 and the low *RMSE*-values.

Then, the corresponding estimated PDFs and scatter plots for f_s and f_c are generated. The associated results are shown in Figs. 13 and 14.

It is evidently found in Figs. 13 and 14 that the estimated PDFs by the X-SVR method highly overlap with the results from the exhaustive MCS. Besides, the accuracy of the virtual models is also intuitively shown by the scatter plots, illustrating that the results by the X-SVR method highly match with the MCS results. Therefore, it is well demonstrated that the developed virtual model is capable of effectively updating the structural responses (i.e., f_s and f_c) and statistical information for the concerned outputs. Then, 7 concerned structural reliability corresponding to distinguish assumed capacities of the system at different statistical information (i.e., $\mu \pm 3\sigma$, $\mu \pm 2\sigma$, $\mu \pm \sigma$, μ), are updated and presented in Table 9.

From Table 9, the concerned statistical probabilities are updated accurately by the established X-SVR virtual models. The accuracy of the implemented X-SVR method is highlighted by the detailed information, i.e., the *RE*s over the concerned probabilities fluctuating between -5.4e-3 % and 5.5e-2 %. Hence, the developed virtual models possess high robustness and are capable of estimating the concerned structural responses under the random variables with multiple distribution types including normal, lognormal, and extreme value distributions.

Subsequently, statistical tests are conducted to demonstrate the capability of the proposed framework to infer means and standard deviations for concerned structural responses when distribution types for random variables are changed. The MCS sample sizes are 5, 10, 25, 50, 75, 100, 150, 300, 550, 700, and 1000, respectively. The convergence studies of the estimated means and standard deviations for f_s and f_c are demonstrated in Figs. 15 and 16.

From Figs. 15 and 16, it can be seen that general convergence trends can be captured when the MCS sample sizes reach 1000, demonstrating the capability of the proposed framework to estimate statistical information for the concerned bandgap properties. Besides, it is necessary to highlight that the estimation of structural reliability by the X-SVR took less than 1 s to update the structural reliability when random variables are modelled as different distribution types. However, FEM-based MCS required more than 270 h to calculate the structural responses with 3e3 iterations, which caused a significantly larger computational burden than the proposed virtual model-aided framework.

5.3. Case B: geometrical uncertainty in the unit cell

Different to the previous Case A, the reliability analysis is conducted in Case B by considering the geometrical uncertainty in the 3D EMM. To construct the effective virtual models through the embedded X-SVR technique, the LHS is employed to generate realizations for the mutually independent inputs within the ranges of [2.85, 3.15] mm for r_a, [11.40, 12.60] mm for r_b, and [0.76, 0.84] mm for r_c. In this case, the material properties are considered as deterministic parameters, with the values of $E = 2$ GPa, $\rho = 1150$ kg/m^3, and $\upsilon = 0.4$. FEM is utilized to compute the corresponding structural responses and the domain discretization in each realization is conducted by the auto-mesh in the FEM software. The brute MCS with 2e3 iterations is conducted as the benchmark to assess the computational accuracy of the established virtual models. With the aid of the convergence study, X-SVR virtual models trained by 100 samples, showing exceptional computational accuracy, and stability, are developed to estimate the structural outputs for f_s and f_c, respectively. Besides, to highlight the computational accuracy of the X-SVR approach, the traditional SVR and NN methods are also implemented for comparison. The performance of the established virtual models is estimated by R^2 and *RMSE*. The associated results are illustrated in Table 10.

From Table 10, superior performance in virtual model construction for both concerned structural responses (i.e., f_s and f_c) can be noticed through the embedded X-SVR technique. Evidentially, in comparison to the traditional SVR and NN, based on the same sets of training samples, the embedded X-SVR models possess higher R^2 values and lower *RMSE* values. Convincingly, based on relatively small training datasets, the X-SVR approach demonstrates high robustness to construct effective virtual models, revealing the

Table 8
Statistics of f_s and f_c by the FEM-based MCS and X-SVR.

		FEM (2e3 iterations)	X-SVR (2e3 iterations)	*RE* (%)
f_s	μ(Hz)	1958.90762	1958.91050	1.47e-4
	σ(Hz)	11.40668	11.42431	1.56e-1
	R^2	N/A	>0.99999	N/A
	RMSE	N/A	0.019085	N/A
f_c	μ(Hz)	7758.59417	7758.60332	1.18e-5
	σ(Hz)	45.12989	45.20060	1.57e-1
	R^2	N/A	>0.99999	N/A
	RMSE	N/A	0.078146	N/A

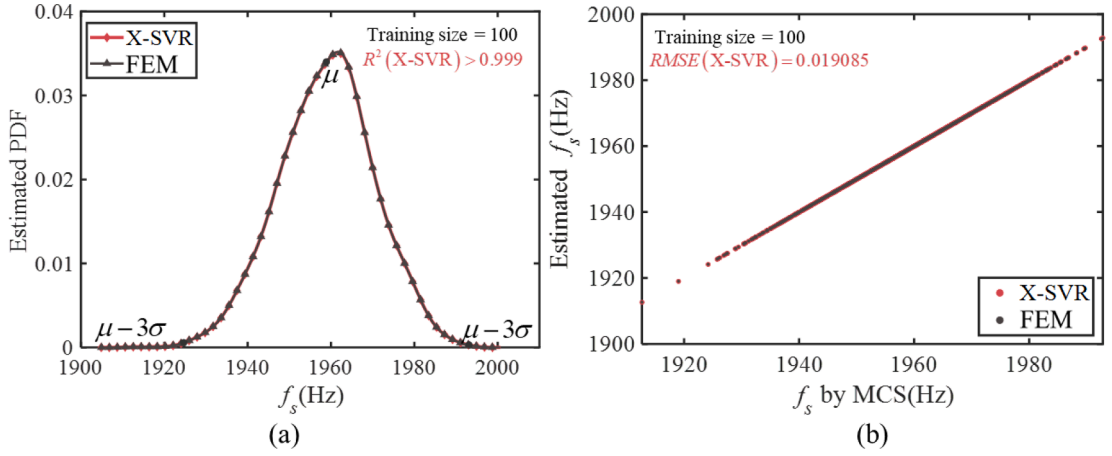

Fig. 13. Estimated (a) PDFs and (b) the scatter plot of f_s under information update.

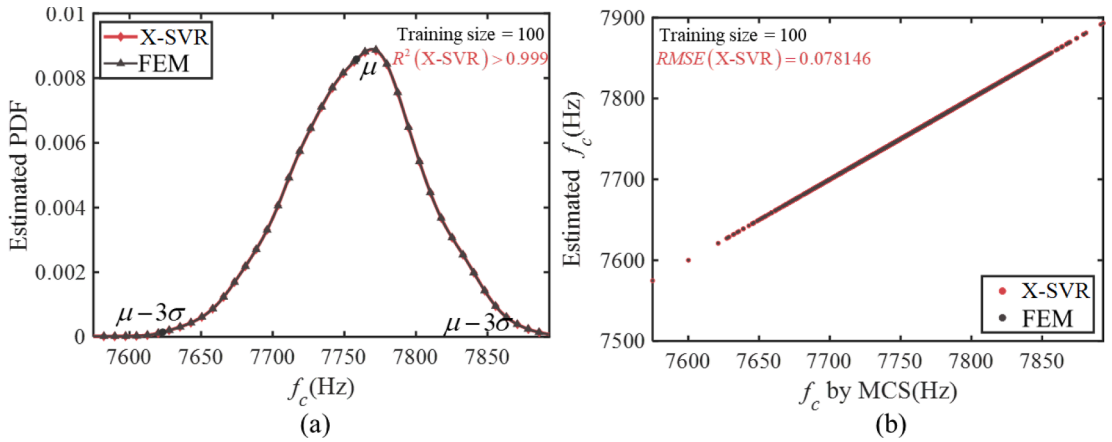

Fig. 14. Estimated (a) PDFs and (b) the scatter plot of f_s under information update.

Table 9
Estimated structural reliability of f_s.

f_s^* (Hz)	$Pr(f_s \leqslant f_s^*)$			
	FEM (2e3 iterations)	X-SVR (2e3 iterations)	*RE* (%)	X-SVR (1e5 iterations)
1924.68758	2.14910e-3	2.14899e-3	-5.4e-3	3.56083e-3
1936.09426	0.026467	0.026479	4.7e-2	0.029915
1947.50094	0.15932	0.15941	5.5e-2	0.16579
1958.90762	0.48204	0.48225	4.3e-2	0.49445
1970.31431	0.83760	0.83773	1.5e-2	0.83464
1981.72099	0.94540	0.94542	2.5e-3	0.97712
1993.12766	0.99938	0.99935	-2.64e-3	0.99870

sophisticated relationship between geometrical parameters and concerned structural responses for the 3D EMM.

By substituting the cumbersome FEM with the explicit virtual models in the following analysis, serious problems that may be raised in the FEM can be avoided, including the time-consuming re-discretization of the domain, re-evaluation of the constitutive relationships with excessive computational burden and computational results with poor quality or even failure in convergence. Accordingly, based on the developed virtual models, an adequate amount of sampling points can be generated in an efficient and effective manner. It provides possible access to the structural reliability for the 3D EMM involving geometrical uncertainty.

Through adopting the LHS to generate more realizations of the uncertainty datasets, corresponding structural responses are estimated by the established virtual models. The PDFs of the concerned structural responses are estimated and shown in Figs. 17 and 18, respectively. The brute MCS with 2e3 iterations are implemented for result verification.

From Figs. 17 and 18, it is found that the estimated PDFs by the X-SVR virtual models highly overlap with the MCS results for both

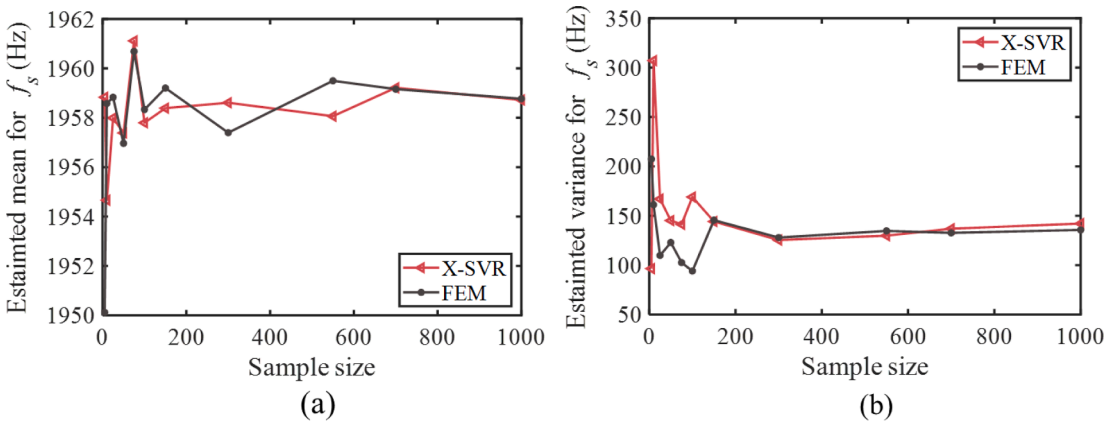

Fig. 15. Convergence plots of the estimated (a) mean and (b) variance for f_s when random variables are following multiple distribution types.

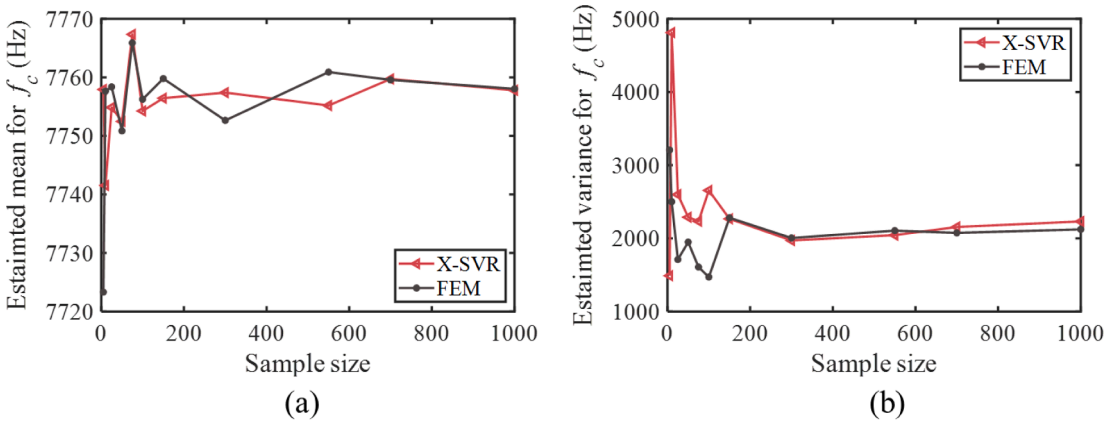

Fig. 16. Convergence plots of the estimated (a) mean and (b) variance for f_c when random variables are following multiple distribution types.

Table 10
Estimated metrics for the trained virtual models.

	f_s			f_c		
	X-SVR	SVR	NN	X-SVR	SVR	NN
Training sample size	100	100	100	100	100	100
R^2	0.99991	0.98182	0.99901	0.99923	0.97056	0.99827
RMSE	0.61194	8.60830	2.05456	8.89021	51.97002	13.36168

quantities of interest. Distinct deviations in the PDFs are noted by the SVR results against the MCS results. Besides, the accuracy of the estimation is further intuitively demonstrated by the scatter plots. From Figs. 17(b) and 18(b), it is noted that obvious dispersion is found between the results from SVR and MCS, especially for the estimation of f_s. In addition, distinct deviations are found between the results from NN and MCS when outputs are around $\mu \pm 3\sigma$. Among these three methods, the X-SVR approach illustrates superior accuracy in estimating the results by the least dispersive data with the MCS results.

Afterwards, the structural reliability is estimated when both f_s^* and f_c^* are set as 7 different values, corresponding to 7 statistical information of μ, $\mu \pm \sigma$, $\mu \pm 2\sigma$, and $\mu \pm 3\sigma$. The results are summarized in Tables 11 and 12.

It is found in Tables 11 and 12 that the trained X-SVR virtual models are competent in estimating the concerned probabilities accurately for both concerned structural responses, by referring to the highly matched estimation between MCS and the X-SVR results. By learning from only 100 training samples, the effective virtual models are established and illustrate exceptional performance in computational accuracy to estimate the adequate statistical information and structural reliability for the 3D EMM considering spatially randomness.

Besides the high accuracy and robustness of the virtual model-aided framework to conduct the reliability analysis considering geometrical uncertainties, it is also worth highlighting the high efficiency with additional statistical data. To estimate the structural

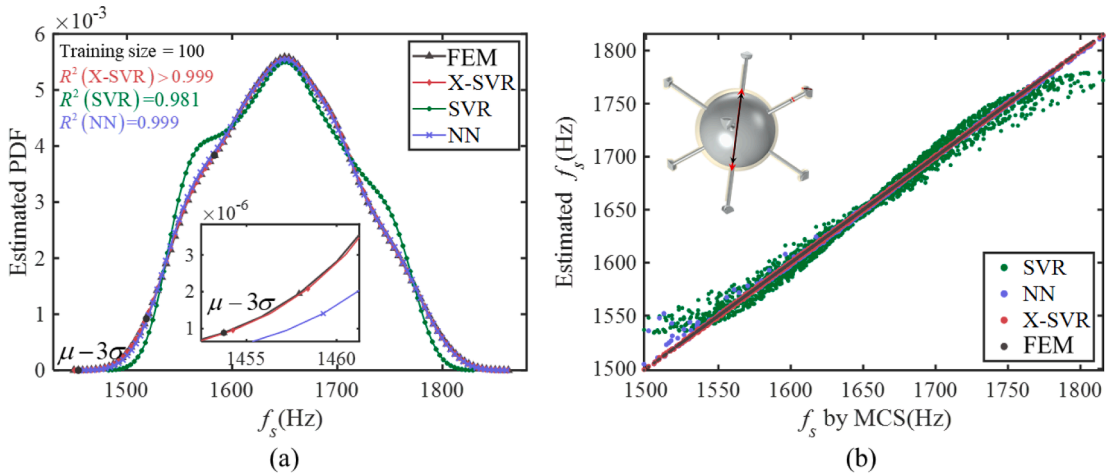

Fig. 17. Estimated (a) PDFs and (b) the scatter plot of f_s for the EMM involving geometrical uncertainties.

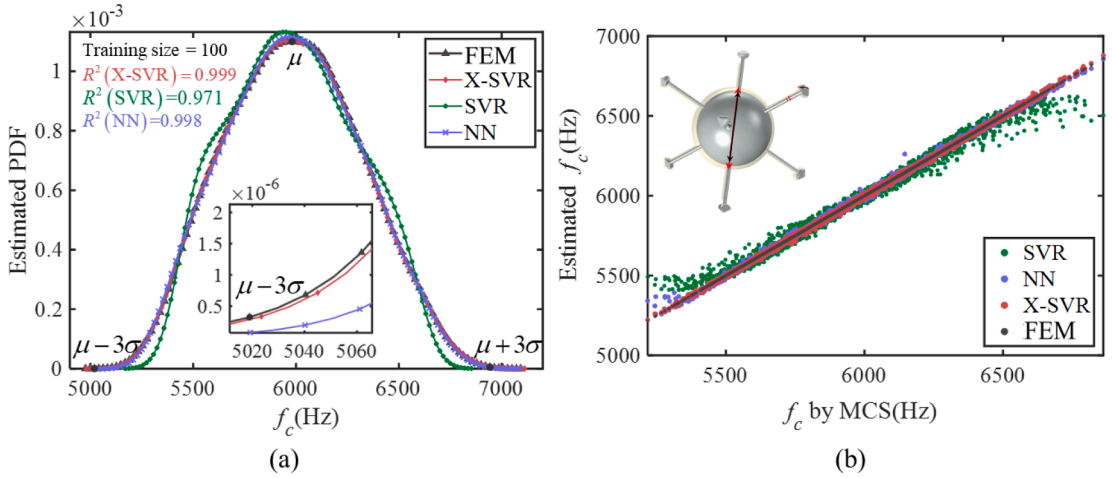

Fig. 18. Estimated (a) PDFs and (b) the scatter plot of f_c for the EMM involving geometrical uncertainties.

Table 11
Structural reliability of f_s.

f_s^e (Hz)	$Pr(f_s \leqslant f_s^e)$			
	FEM (2e3 iterations)	X-SVR (2e3 iterations)	*RE* (%)	X-SVR (1e5 iterations)
1453.81625	4.36638e-6	4.21438e-6	-3.48	<1e-20
1519.32468	0.015198	0.015351	1.01	0.012446
1584.83311	0.18627	0.18680	0.29	0.17158
1650.34154	0.50436	0.50450	0.028	0.50088
1715.84997	0.82068	0.82023	-0.056	0.82000
1781.35840	0.97496	0.97599	0.11	0.97653
1846.86684	0.99995	0.99995	<1e-5	>0.99999

reliability through the proposed virtual model-aided framework, the majority of the computational resources were consumed in the training dataset establishment process. It took 10.28 h to establish the training datasets with 100 sampling points. Subsequently, the estimation of structural reliability with 1e5 iterations took less than 1 s. Nonetheless, the required computational cost to estimate the structural reliability by the FEM-based MCS with 2e3 iterations was 205.6 h. The consumed computational time has been significantly reduced by the proposed framework, which significantly improves the applicability of the brute MCS to conduct the structural reliability analysis for 3D EMMs.

With the aid of the developed virtual models, a local sensitivity analysis, measuring the effects of local perturbations in the random

Table 12
Estimated structural reliability of f_c.

f_c^*(Hz)	$Pr(f_c \leqslant f_c^*)$			
	FEM (2e3 iterations)	X-SVR (2e3 iterations)	*RE* (%)	X-SVR (1e5 iterations)
5024.47535	8.26912e-6	8.47975e-6	2.55	<1e-20
5345.61926	0.015504	0.015547	0.28	0.016377
5666.76316	0.18329	0.18057	-1.49	0.19005
5987.90706	0.50227	0.50149	-0.16	0.52680
6309.05096	0.81901	0.81863	-0.047	0.82307
6630.19486	0.97368	0.97337	-0.0315	0.97351
6951.33876	0.99981	0.99977	-4.11e−3	0.99997

variables on structural reliability, can be conducted efficiently and effectively. In the investigation, r_a, r_b, and r_c are varied in the range from 98 % to 102 % with regard to the nominal values. The associated results are shown in Fig. 19. Besides, the sensitivity index (SIs) [91] measuring the extent of changes in outputs is calculated, which is utilized to identify the critical parameters, affecting significantly on the structural reliability.

Based on the results in Fig. 19, both f_s and f_c are highly sensitive to the uncertainties within r_b and r_c. Significantly lower SIs of r_a are found, especially for f_s, which is less than 15 % of the corresponding SIs of r_b and r_c. Hence, greater effects on structural reliability can be contributed by the uncertainties from r_b and r_c. With the aid of the developed virtual models, the local sensitivity analysis can be conducted with significantly reduced computational time compared with running the reductant FEM models for each distinct realization. Generally, the computational effectiveness, efficiency, and robustness of the proposed virtual model-aided robust reliability analysis, as well as accessory features (e.g., information update and sensitivity analysis), convincingly can benefit the reliability-based design and analysis for 3D EMMs in engineering applications.

5.4. Case C: material and geometrical uncertainties in the unit cell

The respective influences from material and geometrical uncertainties on structural reliability have been revealed in Cases A and B. Considering practical implications, it is common that material and geometrical uncertainties coexist in engineering structures. Therefore, in this case, material and geometrical uncertainties are considered simultaneously in the structural reliability analysis for 3D EMMs. To construct effective virtual models, a training input dataset is generated through LHS when the structural parameters are modelled as mutually independent variables within the ranges of [2.85, 3.15] mm for r_a, [11.40, 12.60] mm for r_b, [0.76, 0.84] mm for r_c, [1.90e9, 2.10e9] Pa for E, [1093.25, 1207.50] kg/m^3 for ρ, and [0.38, 0.42] for υ. The training output dataset is obtained through FEM and the remeshing in each realization is fulfilled by auto-mesh in COMSOL. According to the convergence study, the obvious convergence trends can be captured when the training sample sizes reach 100 for both f_s and f_c. The established virtual models present extraordinary performance in accuracy and computational stability. To further highlight the exceptional performance in virtual model construction, other popular machine learning algorithms, such as SVR and NN are implemented to establish virtual models based on the same training datasets. The performance of the virtual models is assessed based on R^2 and *RMSE*. The corresponding results are shown in Table 13.

In Table 13, it is demonstrated that exceptional performance is achieved in virtual model construction by X-SVR for both f_s and f_c, by learning from 100 training samples. Compared with SVR and NN, virtual models by X-SVR possess higher R^2 and lower *RMSE*, which indicates superior performance in establishing explicit formations for revealing the underpinned relationships between structural parameters, including both material and geometrical parameters, and concerned bandgap properties. Once the virtual models are constructed, f_s and f_c can be estimated based on the established virtual models, which is independent of multiple time-consuming tasks, including domain discretization, meshing, assembly of structural matrix, and evaluation of implicit governing equations. In addition, by integrating the developed virtual models with the sampling-based method, statistical moments, PDFs, and structural reliability can be estimated competently with the extensively reduced computational burden compared with brute MCS coupled with FEM. To demonstrate the high robustness of the X-SVR method in addressing the reliability problem for 3D EMMs, system

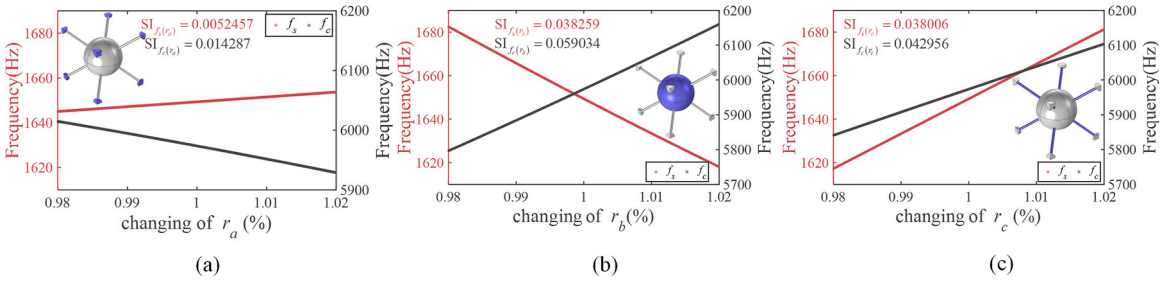

Fig. 19. Local sensitivity analysis of bandgap characteristics with respect to (a) r_a, (b) r_b, and (c) r_c.

Table 13
The estimation metrics for virtual models learnt from 100 sets of training samples.

	f_s			f_c		
	X-SVR	SVR	NN	X-SVR	SVR	NN
R^2	0.99990	0.96256	0.99492	0.99923	0.97659	0.97450
RMSE	0.71980	12.99856	5.13588	10.08214	52.4792	59.9215

uncertainties are modelled as random variables following multiple distribution types. The corresponding statistical information is shown in Table 14.

The accuracy to estimate structural responses by the established virtual models is assessed based on R^2 and *RMSE*. In addition, statistical moments of f_s and f_c are calculated. The exhaustive MCS with 2e3 iterations is employed as the benchmark. The corresponding results are summarized in Table 15.

From Table 15, it is worth noting that the developed virtual models by X-SVR illustrate exceptional performance in computational accuracy for estimating two concerned structural responses, especially for f_c. The R^2 is significantly higher and *RMSE* is extensively lowered of the virtual model by X-SVR compared to SVR and NN. Moreover, *RE*s between MCS and X-SVR for both μ and σ are significantly lower than the corresponding values from SVR and NN. Evidently, the embedded X-SVR method, possessing high robustness, is capable of accurately estimating bandgap characteristics and statistical moments for 3D EMMs involving both material and geometrical uncertainties following multiple distribution types.

Subsequently, the corresponding estimated PDFs and scatter plots for f_s and f_c are presented in Figs. 20 and 21. MCS with 2e3 iterations is conducted as the reference.

From Figs. 20 and 21, it is noteworthy that the estimated PDFs by X-SVR highly match with MCS results. In addition, the accuracy of the estimation by X-SVR is intuitively illustrated by the least dispersive results in reference to MCS results. Therefore, it is convincedly that the adopted X-SVR method can accurately estimate sufficient statistical information, including μ, σ, and PDFs when both material and geometrical uncertainties exist in the 3D EMM. Then, structural reliability corresponding to 7 different values of f_s^* and f_c^*, corresponding to 7 statistical information of μ, $\mu \pm \sigma$, $\mu \pm 2\sigma$, and $\mu \pm 3\sigma$ are estimated. The corresponding results are illustrated in Tables 16 and 17. Results from exhaustive MCS with 2e3 iterations are demonstrated as the reference.

From Tables 16 and 17, by comparing the estimations by FEM and X-SVR both in 2e3 iterations, they are highly matched for both f_s and f_c. However, it should be noted that the computational results in 2e3 iterations have not reached a converged stage. To achieve an acceptable convergence trend, the brute MCS may fail due to the daunting computational costs. Then, our proposed approach provides a feasible solution to extend a much large number of iterations on the established surrogate model. Accordingly, the computational results on the X-SVR model for both f_s and f_c in 1e5 iterations are also presented in Tables 16 and 17.

Besides the high robustness and accuracy of the developed framework, the high efficiency of the proposed framework is highlighted with more statistical data. It consumed 211.18 h to conduct structural reliability analysis through exhaustive MCS with 2e3 iterations. Nonetheless, by employing virtual model-aided framework, the majority of time is consumed by the training dataset generation process, which took 10.56 h to construct the training dataset with 100 sampling points. Then, the estimation of structural reliability with 1e5 iterations required less than 1 s. Hence, it is clearly illustrated that the computational cost is extensively reduced in the virtual model-aided approach, implying the significantly improved applicability to conduct structural reliability analysis for 3D EMMs.

Apart from the merits of the framework, it is worth emphasizing that the accuracy of failure probability estimation by the proposed approach on the 3D EMM is influenced by the structural capacity. Implementing the proposed framework for estimating failure probability concerning rare events requires careful consideration. Moreover, one assumption in the numerical investigation is that the uncertainties of each unit cell in 3D EMMs are identical, which is not practical in real-life scenarios. The investigation in this paper provides an approximation of structural reliability for 3D EMMs. Future works investigating structural reliability for EMMs with supercells or metastructures with spatial variations are required for accurate estimation of failure probability for 3D practical EMMs.

6. Conclusion

A novel virtual model-aided framework is proposed in this paper to estimate the structural reliability for 3D EMMs involving both material and geometrical randomness. A supervised kernel-based virtual modelling technique, namely the extended support vector regression (X-SVR) is embedded into the approach to establish effective virtual models that depict the underpinned and sophisticated

Table 14
Statistical information of material and geometrical uncertainties.

Random variable	Distribution type	μ	σ	Range
r_a(mm)	Gamma	3.00	0.03	2.85–3.15
r_b(mm)	Normal	12.00	0.12	11.40–12.60
r_c(mm)	Extreme value	0.8	0.005	0.76–0.84
E(GPa)	Logistic	2.00	0.015	1.9–2.1
ρ(kg/m^3)	Lognormal	1150	11.5	1.09–1.21
υ	Lognormal	0.4	0.004	0.38–0.42

Table 15
Statistics of f_s and f_c by MCS, X-SVR, SVR, and NN when sampling size is 2e3 iterations. (Unit Hz).

		FEM	X-SVR	*RE* (%)	SVR	*RE* (%)	NN	*RE* (%)
f_s	μ	1644.8184	1644.8534	2.1e-3	1640.6020	0.26	1647.1754	0.14
	σ	21.3571	21.3390	-0.060	25.6223	20.0010	20.3418	-4.73
	R^2	N/A	0.9993	N/A	0.9465	N/A	0.9720	N/A
	RMSE	N/A	0.5481	N/A	6.1753	N/A	3.4763	N/A
f_c	μ	5955.7534	5958.9650	0.054	5930.1108	-0.43	5966.5354	0.18
	σ	107.9151	108.2019	0.2908	139.7218	29.474	124.8680	15.74
	R^2	N/A	0.9932	N/A	0.9187	N/A	0.9270	N/A
	RMSE	N/A	8.9562	N/A	42.2359	N/A	30.0146	N/A

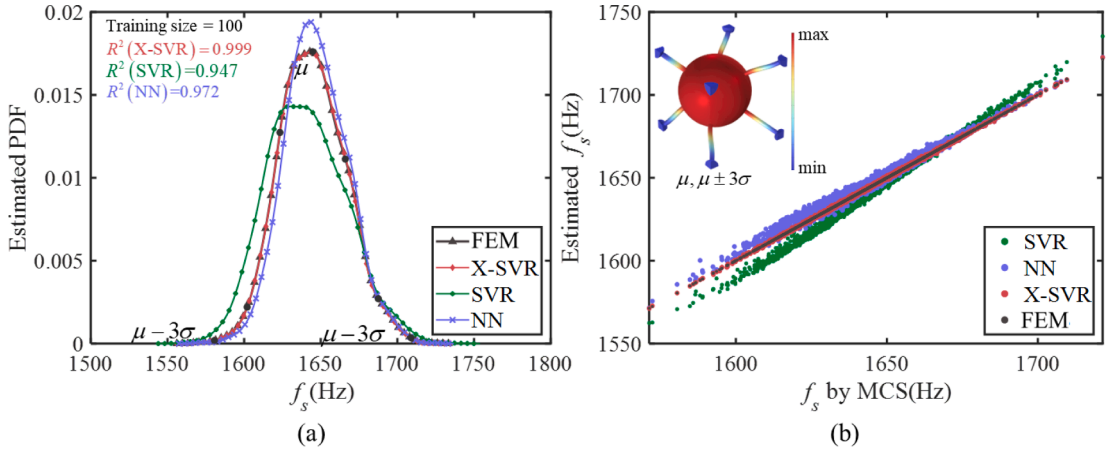

Fig. 20. Estimated (a) PDFs and (b) the scatter plot of f_s for the EMM with material and geometrical uncertainties simultaneously.

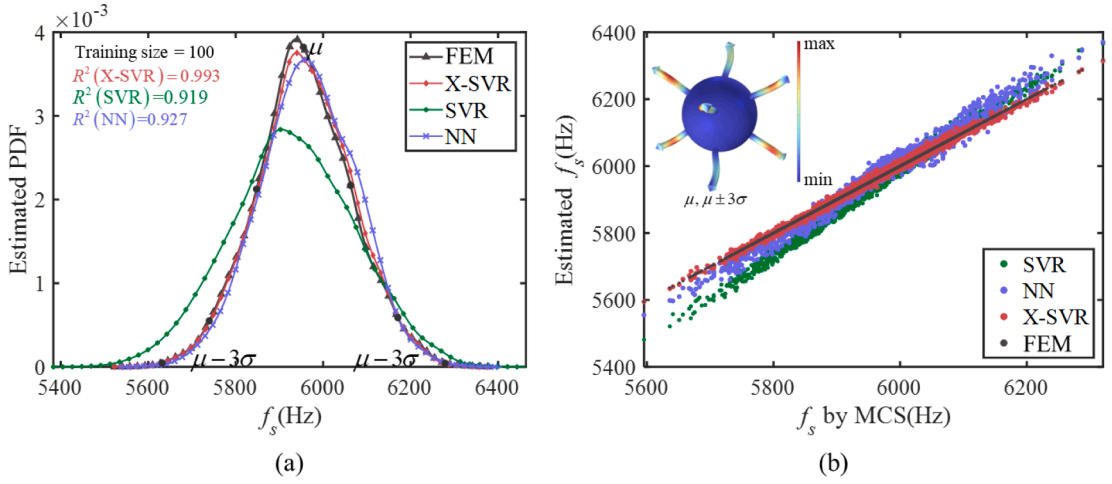

Fig. 21. Estimated (a) PDFs and (b) the scatter plot of f_c for the EMM with material and geometrical uncertainties simultaneously.

relationships between system uncertainties and the concerned structural responses. Then, the Monte Carlo simulation (MCS) is implemented on the established virtual models to estimate adequate statistical information and structural reliability in an effective and efficient manner. Distinct from the brute MCS coupled with the finite element method (FEM), such a calculation scheme can be partially independent of the cumbersome domain discretization, the structural matrix assembly, and the sophisticated constitutive relationship evaluation, which are often the nest of computational burdens or even errors.

The high robustness, accuracy, and efficiency of the X-SVR technique are highlighted in three numerical investigation cases, which analyze structural reliability considering material and geometrical uncertainties separately and simultaneously. Furthermore, once the virtual models are established, information update and the sensitivity analysis can be fulfilled easily. Convincingly, the proposed virtual model-aided framework with high robustness and applicability can tackle the reliability analysis for EMMs efficiently and

Table 16
Estimated structural reliability of f_s.

Probability	FEM (2e3 iterations)	X-SVR (2e3 iterations)	*RE* (%)	X-SVR (1e5 iterations)
$Pr(f_s \leqslant 1580.7471)$	1.61631e-3	1.59170e-3	-1.52	2.15238e-3
$Pr(f_s \leqslant 1602.1042)$	0.019158	0.019300	0.74	0.025078
$Pr(f_s \leqslant 1623.4613)$	0.16185	0.16177	-0.049	0.15608
$Pr(f_s \leqslant 1644.8184)$	0.51243	0.51076	-0.33	0.49158
$Pr(f_s \leqslant 1666.1755)$	0.82697	0.82906	0.25	0.83492
$Pr(f_s \leqslant 1687.5326)$	0.96881	0.96848	-0.034	0.97556
$Pr(f_s \leqslant 1708.8897)$	0.99804	0.99806	2.00e-3	0.99851

Table 17
Estimated structural reliability of f_c.

Probability	FEM (2e3 iterations)	X-SVR (2e3 iterations)	*RE* (%)	X-SVR (1e5 iterations)
$Pr(f_c \leqslant 5632.0081)$	1.23370e-3	1.21361e-3	-1.63	1.61630e-3
$Pr(f_c \leqslant 5739.9232)$	0.025073	0.024472	-2.40	0.023333
$Pr(f_c \leqslant 5847.8383)$	0.15984	0.15743	-1.51	0.15783
$Pr(f_c \leqslant 5955.7534)$	0.50709	0.49205	-2.97	0.49545
$Pr(f_c \leqslant 6063.6685)$	0.83502	0.82686	-0.98	0.83568
$Pr(f_c \leqslant 6171.5836)$	0.97070	0.97179	0.11	0.97501
$Pr(f_c \leqslant 6279.4987)$	0.99860	0.99864	4.01e-3	0.99835

effectively, offering extensive merits on the structural analysis, design, and application of them with high reliability in multi-disciplinary engineering.

CRediT authorship contribution statement

Minghui Zhang: Conceptualization, Formal analysis, Investigation, Methodology, Software, Validation, Writing – original draft. **Qihan Wang:** Conceptualization, Methodology, Software, Writing – review & editing. **Zhen Luo:** Conceptualization, Funding acquisition, Writing – review & editing. **Wei Gao:** Conceptualization, Funding acquisition, Supervision, Writing – review & editing.

Declaration of competing interest

The authors declare that they have no known competing financial interests or personal relationships that could have appeared to influence the work reported in this paper.

Data availability

Data will be made available on request.

Acknowledgement

The work presented in this paper has been supported by Australian Research Council projects IH210100048, IH200100010, DP210101353, and DP240102559.

References

[1] W.J. Padilla, D.N. Basov, D.R. Smith, Negative refractive index metamaterials, Mater. Today 9 (7–8) (2006) 28–35.
[2] J. Valentine, et al., Three-dimensional optical metamaterial with a negative refractive index, Nature 455 (7211) (2008) 376–379.
[3] R. Marqués, F. Medina, R. Rafii-El-Idrissi, Role of bianisotropy in negative permeability and left-handed metamaterials, Phys. Rev. B 65 (14) (2002) 144440.
[4] N.J. Engheta, An idea for thin subwavelength cavity resonators using metamaterials with negative permittivity and permeability, IEEE Antennas Wireless Propagation Lett. 1 (2002) 10–13.
[5] M. Zhang, Y. Xiao, Q.-H. Qin, Modal-based analysis for aiding 3d elastic metastructure design, Int. J. Appl. Mech. 15 (7) (2023) 2350058.
[6] G. Ma, P. Sheng, Acoustic metamaterials: From local resonances to broad horizons, Sci. Adv. 2 (2) (2016) e1501595.
[7] H. Chen, C.T. Chan, Acoustic cloaking in three dimensions using acoustic metamaterials, Appl. Phys. Lett. 91 (18) (2007).
[8] Z. Yang, et al., Membrane-type acoustic metamaterial with negative dynamic mass, Phys. Rev. Lett. 101 (20) (2008) 204301.
[9] G. Hu, et al., Metamaterial beam with graded local resonators for broadband vibration suppression, Mech. Syst. Signal Process. 146 (2021) 106982.
[10] Z. Liu, et al., Locally resonant sonic materials, Science 289 (5485) (2000) 1734–1736.
[11] M. Zhang, et al., Design of elastic metamaterials with ultra-wide low-frequency stopbands via quantitative local resonance analysis, Thin-Walled Struct. 165 (2021) 107969.
[12] Q. Wang, et al., Bandgap properties in metamaterial sandwich plate with periodically embedded plate-type resonators, Mech. Syst. Signal Process. 151 (2021) 107375.

[13] Z. Liu, R. Rumpler, L. Feng, Locally resonant metamaterial curved double wall to improve sound insulation at the ring frequency and mass-spring-mass resonance, Mech. Syst. Signal Process. 149 (2021) 107179.
[14] Y. Wang, D.L. McDowell, Uncertainty quantification in multiscale materials modeling, Woodhead Publishing, 2020.
[15] N. Korshunova, et al., Uncertainty quantification of microstructure variability and mechanical behavior of additively manufactured lattice structures, Comput. Methods Appl. Mech. Eng. 385 (2021) 114049.
[16] Q. Wang, et al., Polymorphic uncertainty quantification for engineering structures via a hyperplane modelling technique, Comput. Methods Appl. Mech. Eng. 398 (2022) 115250.
[17] D. Yao, et al., Flexural wave mitigation in metamaterial cylindrical curved shells with periodic graded arrays of multi-resonator, Mech. Syst. Signal Process. 168 (2022) 108721.
[18] X. Yin, et al., Bandgap characteristics of a tensegrity metamaterial chain with defects, Extreme Mech. Lett. 36 (2020) 100668.
[19] S.C. Fischer, L. Hillen, C. Eberl, Mechanical metamaterials on the way from laboratory scale to industrial applications: Challenges for characterization and scalability, Materials 13 (16) (2020) 3605.
[20] E. Bachy, et al., Investigations on the performance and the robustness of a metabsorber designed for structural vibration mitigation, Mech. Syst. Signal Process. 170 (2022) 108830.
[21] L. Mathelin, M.Y. Hussaini, T.A. Zang, Stochastic approaches to uncertainty quantification in CFD simulations, Numer. Algorithms 38 (2005) 209–236.
[22] H.P. Gavin, S.C. Yau, High-order limit state functions in the response surface method for structural reliability analysis, Struct. Saf. 30 (2) (2008) 162–179.
[23] Q. Wang, et al., Machine learning aided static structural reliability analysis for functionally graded frame structures, App. Math. Model. 78 (2020) 792–815.
[24] K. Yang, H. Younis, A semi-analytical Monte Carlo simulation method for system's reliability with load sharing and damage accumulation, Reliab. Eng. Syst. Saf. 87 (2) (2005) 191–200.
[25] G. Stefanou, The stochastic finite element method: past, present and future, Comput. Methods Appl. Mech. Eng. 198 (9–12) (2009) 1031–1051.
[26] R. Ghanem, Ingredients for a general purpose stochastic finite elements implementation, Comput. Methods Appl. Mech. Eng. 168 (1–4) (1999) 19–34.
[27] Z. Zheng, et al., A stochastic finite element scheme for solving partial differential equations defined on random domains, Comput. Methods Appl. Mech. Eng. 405 (2023) 115860.
[28] N.-Z. Chen, C.G. Soares, Spectral stochastic finite element analysis for laminated composite plates, Comput. Methods Appl. Mech. Eng. 197 (51–52) (2008) 4830–4839.
[29] Z. He, J. Hu, E. Li, An uncertainty model of acoustic metamaterials with random parameters, Comput. Mech. 62 (2018) 1023–1036.
[30] J. Henneberg, et al., Periodically arranged acoustic metamaterial in industrial applications: The need for uncertainty quantification, Appl. Acoust. 157 (2020) 107026.
[31] M. Ben Souf, et al., On the variability of the sound transmission loss of composite panels through a parametric probabilistic approach, J. Comput Acoust. 24 (01) (2016) 1550018.
[32] P. Zakian, N. Khaji, A stochastic spectral finite element method for wave propagation analyses with medium uncertainties, App. Math. Model. 63 (2018) 84–108.
[33] J. Jung, et al., Realisation of a locally resonant metamaterial on the automobile panel structure to reduce noise radiation, Mech. Syst. Signal Process. 122 (2019) 206–231.
[34] J. Fan, et al., A review of additive manufacturing of metamaterials and developing trends, Mater. Today 50 (2021) 303–328.
[35] Z. Liu, C.T. Chan, P. Sheng, Analytic model of phononic crystals with local resonances, Phys. Rev. B 71 (1) (2005) 014103.
[36] F. Lucklum, M.J. Vellekoop, Bandgap engineering of three-dimensional phononic crystals in a simple cubic lattice, Appl. Phys. Lett. 113 (20) (2018).
[37] R.G. Ghanem, P.D. Spanos, Spectral stochastic finite-element formulation for reliability analysis, J. Eng. Mech. 117 (10) (1991) 2351–2372.
[38] Z. Zhu, X. Du, Reliability analysis with Monte Carlo simulation and dependent Kriging predictions, J. Mech. Des. 138 (12) (2016) 121403.
[39] C. Luo, et al., Hybrid enhanced Monte Carlo simulation coupled with advanced machine learning approach for accurate and efficient structural reliability analysis, Comput. Methods Appl. Mech. Eng. 388 (2022) 114218.
[40] W. Dong, et al., An artificial intelligence-based conductivity prediction and feature analysis of carbon fiber reinforced cementitious composite for non-destructive structural health monitoring, Eng. Struct. 266 (2022) 114578.
[41] V.-H. Truong, et al., Evaluation of machine learning models for load-carrying capacity assessment of semi-rigid steel structures, Eng. Struct. 273 (2022) 115001.
[42] Q. Wang, et al., Machine learning aided stochastic structural free vibration analysis for functionally graded bar-type structures, Thin-Walled Struct. 144 (2019) 106315.
[43] F. Farzbod, O.E. Scott-Emuakpor, Interactions beyond nearest neighbors in a periodic structure: Force analysis, Int. J. Solids Struct. 199 (2020) 203–211.
[44] F. Farzbod, Number of wavevectors for each frequency in a periodic structure, J. Vibr. Acoust. 139 (5) (2017) 051006.
[45] K. Wang, et al., Nonlocal interaction engineering of 2D roton-like dispersion relations in acoustic and mechanical metamaterials, Commun. Mater. 3 (1) (2022) 35.
[46] Y. Chen, M. Kadic, M. Wegener, Roton-like acoustical dispersion relations in 3D metamaterials, Nat. Commun. 12 (1) (2021) 3278.
[47] X. Fei, et al., Three-dimensional anti-chiral auxetic metamaterial with tunable phononic bandgap, Appl. Phys. Lett. 116 (2) (2020).
[48] D'Alessandro, L., et al., Low frequency 3D ultra-wide vibration attenuation via elastic metamaterial. 2019. 9(1): p. 8039.
[49] M. Collet, et al., Floquet-Bloch decomposition for the computation of dispersion of two-dimensional periodic, damped mechanical systems, Int. J. Solids Struct. 48 (20) (2011) 2837–2848.
[50] H. Jiang, et al., Band gaps and vibration isolation of a three-dimensional metamaterial with a star structure, Materials 13 (17) (2020) 3812.
[51] W. Setyawan, S. Curtarolo, High-throughput electronic band structure calculations: challenges and tools, Comput. Mater. Sci 49 (2) (2010) 299–312.
[52] A. Der Kiureghian, Analysis of structural reliability under parameter uncertainties, Probab. Eng. Mech. 23 (4) (2008) 351–358.
[53] M.G. Stewart, M.D. Netherton, Security risks and probabilistic risk assessment of glazing subject to explosive blast loading, Reliab. Eng. Syst. Saf. 93 (4) (2008) 627–638.
[54] P. Thoft-Cristensen, M.J. Baker, Structural Reliability Theory and its Applications, Springer Science & Business Media, 2012.
[55] R.E. Melchers, A.T. Beck, Structural Reliability Analysis and Prediction, John wiley & sons, 2018.
[56] B.J. Bichon, J.M. McFarland, S. Mahadevan, Efficient surrogate models for reliability analysis of systems with multiple failure modes, Reliab. Eng. Syst. Saf. 96 (10) (2011) 1386–1395.
[57] W. Gao, et al., Structural reliability analysis with imprecise random and interval fields, App. Math. Model. 55 (2018) 49–67.
[58] D. Wu, W. Gao, Hybrid uncertain static analysis with random and interval fields, Comput. Methods Appl. Mech. Eng. 315 (2017) 222–246.
[59] M. Papadrakakis, V. Papadopoulos, Robust and efficient methods for stochastic finite element analysis using Monte Carlo simulation, Comput. Methods Appl. Mech. Eng. Structures 134 (3–4) (1996) 325–340.
[60] A. Shapiro, T. Homem-de-Mello, On the rate of convergence of optimal solutions of Monte Carlo approximations of stochastic programs, SIAM J. Optim. 11 (1) (2000) 70–86.
[61] W. Gao, C. Song, F. Tin-Loi, Probabilistic interval analysis for structures with uncertainty, Struct. Saf. 32 (3) (2010) 191–199.
[62] E. Lofrano, A. Paolone, M. Vasta, A perturbation approach for the identification of uncertain structures, Int. J. Dyn. Control 4 (2016) 204–212.
[63] X. Liu, et al., Extended Wittrick-Williams algorithm for eigenvalue solution of stochastic dynamic stiffness method, Mech. Syst. Signal Process. 166 (2022) 108354.
[64] B. Van den Nieuwenhof, J.-P. Coyette, Modal approaches for the stochastic finite element analysis of structures with material and geometric uncertainties, Comput. Methods Appl. Mech. Eng. 192 (33–34) (2003) 3705–3729.
[65] D.M. Ghiocel, R.G. Ghanem, Stochastic finite-element analysis of seismic soil–structure interaction, J. Eng. Mech. 128 (1) (2002) 66–77.
[66] J.D. Arregui-Mena, L. Margetts, P.M. Mummery, Practical application of the stochastic finite element method, Arch. Comput. Meth. Eng. 23 (2016) 171–190.

[67] M. Dunbar, et al., Simultaneous classification and feature selection via convex quadratic programming with application to HIV-associated neurocognitive disorder assessment, Eur. J. Oper. Res. 206 (2) (2010) 470–478.
[68] D. Wipf, S. Nagarajan, A new view of automatic relevance determination, Adv. Neural Inf. Proces. Syst. 20 (2007).
[69] V. Vapnik, The support vector method of function estimation, in: Nonlinear Modeling: Advanced Black-Box Techniques, Springer, 1998, pp. 55–85.
[70] Schölkopf, B. and A.J. Smola, Learning with kernels: support vector machines, regularization, optimization, and beyond. 2002: MIT press.
[71] Hofmann, T., B. Schölkopf, and A.J. Smola, Kernel methods in machine learning. 2008.
[72] C. Campbell, Y. Ying, Learning with support vector machines, Springer Nature, 2022.
[73] Hensman, J., et al., Gaussian processes for big data. arXiv preprint arXiv:1309.6835, 2013.
[74] J. Wang, Y. Ma, L. Ouyang, et al., Bayesian modeling and optimization for multi-response surfaces, Comput. Ind. Eng. 142 (2020) 106357.
[75] Ye, N., et al. Support vector machine with orthogonal Chebyshev kernel. in 18th International Conference on Pattern Recognition (ICPR'06). 2006. IEEE.
[76] Klein, A., et al. Fast bayesian optimization of machine learning hyperparameters on large datasets. in Artificial intelligence and statistics. 2017. PMLR.
[77] H. Cho, et al., Basic enhancement strategies when using Bayesian optimization for hyperparameter tuning of deep neural networks, IEEE Access 8 (2020) 52588–52608.
[78] M. Cieslak, et al., Quasi-Monte Carlo simulation of the light environment of plants, Funct. Plant Biol. 35 (10) (2008) 837–849.
[79] A.M. Olsson, G.E. Sandberg, Latin hypercube sampling for stochastic finite element analysis, J. Eng. Mech. 128 (1) (2002) 121–125.
[80] A. Afzal, et al., Effects of Latin hypercube sampling on surrogate modeling and optimization, Int. J. Fluid Mach. Syst. 10 (3) (2017) 240–253.
[81] R.L. Iman, Latin hypercube sampling, Encycl. Quant. Risk Anal. Assess. (2008) 3.
[82] B. Minasny, A.B. McBratney, A conditioned Latin hypercube method for sampling in the presence of ancillary information, Comput. Geosci. 32 (9) (2006) 1378–1388.
[83] Sharma, N. and K. Saroha. Study of dimension reduction methodologies in data mining. in International Conference on Computing, Communication & Automation. 2015. IEEE.
[84] T. Jayalakshmi, A. Santhakumaran, Statistical normalization and back propagation for classification, Int. J. Comput. Theory Eng. Struct. 3 (1) (2011) 1793–8201.
[85] S. Theocharides, et al., Day-ahead photovoltaic power production forecasting methodology based on machine learning and statistical post-processing, Appl. Energy 268 (2020) 115023.
[86] M. Paluszek, S. Thomas, MATLAB Machine Learning, Apress, 2016.
[87] R. Zhu, et al., A chiral elastic metamaterial beam for broadband vibration suppression, J. Sound Vibr. 333 (10) (2014) 2759–2773.
[88] H. Pradlwarter, et al., Application of line sampling simulation method to reliability benchmark problems, Struct. Saf. 29 (3) (2007) 208–221.
[89] M.D. Pandey, X. Zhang, System reliability analysis of the robotic manipulator with random joint clearances, Mech. Mach. Theory 58 (2012) 137–152.
[90] N.M. Pindoriya, et al., Composite reliability evaluation using Monte Carlo simulation and least squares support vector classifier, IEEE Trans. Power Syst. 26 (4) (2011) 2483–2490.
[91] G. Qian, A. Mahdi, Sensitivity analysis methods in the biomedical sciences, Math. Biosci. 323 (2020) 108306.
[92] M. Zhang, et al., Stochastic bandgap optimization for multiscale elastic metamaterials with manufacturing imperfections, Int. J. Mech. Sci. (2024) 109035.